EXAMINING A HYPERSONIC TURBULENT BOUNDARY LAYER AT LOW REYNOLDS NUMBER

A Dissertation

by

MICHAEL THOMAS SEMPER

Submitted to the Office of Graduate Studies of
Texas A&M University
in partial fulfillment of the requirements for the degree of

DOCTOR OF PHILOSOPHY

Chair of Committee,	Rodney Bowersox
Committee Members,	Sharath Girimaji
	Simon North
	Othon Rediniotis
Head of Department,	Rodney Bowersox

August 2013

Major Subject: Aerospace Engineering

ABSTRACT

The purpose of the current study was to answer several questions related to hypersonic, low Reynolds number, turbulent boundary layers, of which available data related to turbulence quantities is scarce. To that end, a unique research facility was created, instrumentation was developed to acquire data in the challenging low Reynolds number (low density) domain, and meaningful data was collected and analyzed. The low Reynolds number nature of the boundary layer ($Re_\theta = 3700$) allows for tangible DNS computations/validations using the current geometry and conditions. The boundary layer examined in this experiment resembled other, higher Reynolds number boundary layers, but also exhibited its own unique characteristics.

The Van Driest equivalent velocity scaling method was found to perform well, and the log layer of the law of the wall plot matched expected theory. Noticeably absent from the data was an overlap region between the two layers, which suggests a different profile for the velocity profiles at these low Reynolds number, hypersonic conditions. The low density effects near the wall may be having an effect on the turbulence that modifies this region in a manner not currently anticipated. The Crocco-Busemann relation was found to provide satisfactory results under its general assumptions.

When compared to available data, the Morkovin scaled velocity fluctuations fell almost an order of magnitude short. Currently, it is not known if this deficit is due to inadequacies with the Strong Reynolds Analogy, or the Morkovin scaling parameters.

The trips seem to promote uniformity across the span of the model, and the data seems to generally be in agreement across the spanwise stations. However, additional information is needed to determine if two-dimensional simulations are sufficient for these boundary layers.

When the turbulent boundary layer power spectra is analyzed, the result is found to follow the traditional power law. This result verifies that even at low Reynolds numbers, the length scales still follow the behavior described by Kolmogorov.

Moving downstream of the trips, the peak RMS disturbance value grows in amplitude until it reaches a critical value. After this point, the peak begins to decrease in amplitude, but the affected region spreads throughout the boundary layer. Once the influenced region covers a significant portion of the boundary layer, transition occurs.

DEDICATION

This dissertation is dedicated to all my friends and family who supported me throughout my long campaign.

ACKNOWLEDGEMENTS

I would like to gratefully acknowledge first and foremost all of my colleagues at the lab who helped me throughout the years. Despite all the setbacks, they were always there to help me continue on and end on a high note.

Second, I would like to thank Dr. Bowersox for recruiting me to help build our lab from the ground up, and pushing me to continue my research and create something of which I am truly proud.

I would also like to acknowledge my committee who have taken the time to review my work and provide useful commentary.

Finally, I would like to acknowledge the sponsors that funded myself and my research, both Dr. John Schmisseur of the AFOSR on the original MURI grant, and NASA from the hypersonic research center.

NOMENCLATURE

Common Symbols

c_p	specific heat at constant pressure, $kJ/(kg-K)$
c_v	specific heat at constant volume, $kJ/(kg-K)$
$\mathbf{g}$	gravity, m/s^2
h	enthalpy, kJ/kg
k	thermal conductivity, $W/(m-K)$
L	characteristic length, m
M	Mach number
Nu	Nusselt number
P	pressure, Pa
r	recovery temperature, T_w/T_{aw}
Re	Reynolds number, $\rho uL/\mu$
Re_d	Reynolds number based on wire diameter
Re_x	Reynolds number at a specific location, x
Re_θ	Reynolds number based on momentum thickness
t	time, s
T	temperature, K
T_{wire}	hotwire temperature, K
u	streamwise velocity, m/s
u^+	inner variable scaled velocity
$\mathbf{V}$	velocity vector, m/s

x	streamwise length, m
y	wall normal distance, m
y^+	inner variable scaled wall normal distance
z	spanwise direction, m

Greek Symbols

δ	boundary layer thickness, m
δ^*	displacement thickness, m
γ	ratio of specific heats
η	hotwire recovery ratio
μ	dynamic viscosity, $Pa \cdot s$
ρ	density, kg/m^3
τ	hotwire overheat ratio, T_{wire}/T_t
θ	momentum thickness, m
Ω	resistance, Ohms

Common Subscripts

aw	adiabatic wall
e	edge conditions
t	total conditions
w	wall conditions
∞	freestream conditions

Acronyms

ACE	Actively Controlled Expansion
APG	adverse pressure gradient
CFD	computational fluid dynamics
DNS	direct numerical simulation
LDV	laser doppler velocimetry
LES	large eddy simulation
MTV	molecular tagging velocimetry
OHR	overheat ratio (see τ)
PIV	particle image velocimetry
$PLIF$	planar laser induced fluorescence
$RANS$	Reynolds averaged Navier Stokes
RMS	root-mean square
$SBLI$	shock boundary layer interaction
SRA	Strong Reynolds Analogy
$VENOM$	Vibrationally Enhanced Nitric Oxide Monitoring
ZPG	zero pressure gradient

TABLE OF CONTENTS

LIST OF FIGURES

FIGURE Page

LIST OF TABLES

TABLE Page

1. INTRODUCTION

Hypersonic flow is sometimes singularly characterized by a Mach number greater than 5. However, this criterion alone fails to capture the many dynamics and interactions that occur at high speeds as opposed to the lower speed regimes. Hypersonic flow generates thin shock layers, thick entropy layers, highly coupled viscous interactions between shock waves and boundary layers, low density effects, and at higher Mach numbers, high temperature effects where real gas calculations, nonequilibrium flow, and chemical reactions become important[2]. All of these physical effects are shown on a typical hypersonic flight vehicle in Figure 1.1. The introduction of new flow physics requires refinement in predictive and analytic tools, and in some cases necessitates entirely new models or theories to be developed.

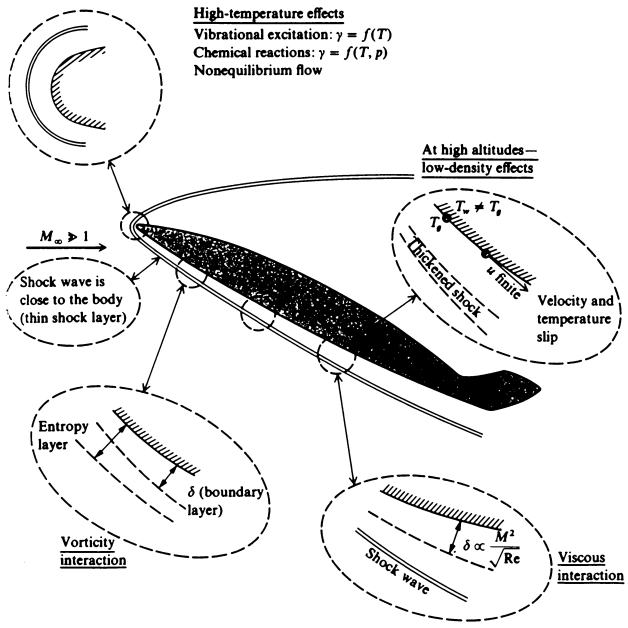

Figure 1.1: Hypersonic Vehicle and Associated Flowfield (Ref. 2)

An important note on hypersonic flows is that the higher Mach numbers associated with these conditions do not necessarily translate to higher Reynolds numbers (Reynolds number is the dimensionless quantity representing the ratio of inertial forces to viscous forces). Hypersonic vehicles are generally designed for high-altitude purposes, or even access to space. These specialized flight envelopes therefore typically exist at densities far lower than subsonic and supersonic vehicles. Indeed, there are those specific points where the Reynolds number of a hypersonic vehicle may be equal to or lower than that of a transonic aircraft. As an example, see Figure 1.2 which highlights several hypersonic vehicles on a Mach number versus altitude map. Also included in the figure are the current facilities available at the Texas A&M University National Aerothermochemistry Laboratory. However, the strong shock waves that hypersonic vehicles encounter ahead of their path create new challenges in chemical-gas kinetics and heat transfer. Because these temperatures can often be orders of magnitude higher than subsonic (or even supersonic) flows, the necessity to accurately predict and design for these conditions becomes an order of magnitude more important. And while low density flows and (in some cases) large areas of laminar flow across a vehicle may seem ideal from a drag perspective, they nonetheless create problems caused by insufficient control surface area, flow separation across vehicle geometry changes, and mixing inefficiencies in air-breathing hypersonic propulsion vehicles.

As aerodynamic knowledge has become stronger over time, new tools have been developed both in the form of more robust computational solvers and more encompassing empirical relations. These solvers and relations were (and still are) refined as the march in to the supersonic regime continued. In some cases, simple scaling laws allowed low speed relations to be applied to higher speed cases, and other times new theories and data sets were utilized to develop new models or empirical

relations. Now, as hypersonic flight becomes more important in today's research, the community finds itself once again building on available knowledge to improve its understanding for future designs. As will be discussed more in Section 2.4, there are many reasons to expect low Reynolds number hypersonic flows to differ from high Reynolds number supersonic flows. For a qualitative example, see Figure 1.3. Figure 1.3a represents a high Reynolds number boundary layer visualization, and Figure 1.3b is an analogous image at low Reynolds number taken in the current facility. It would appear by simple comparison of the two images that even the basic instantaneous structure of the two boundary layers is significantly different

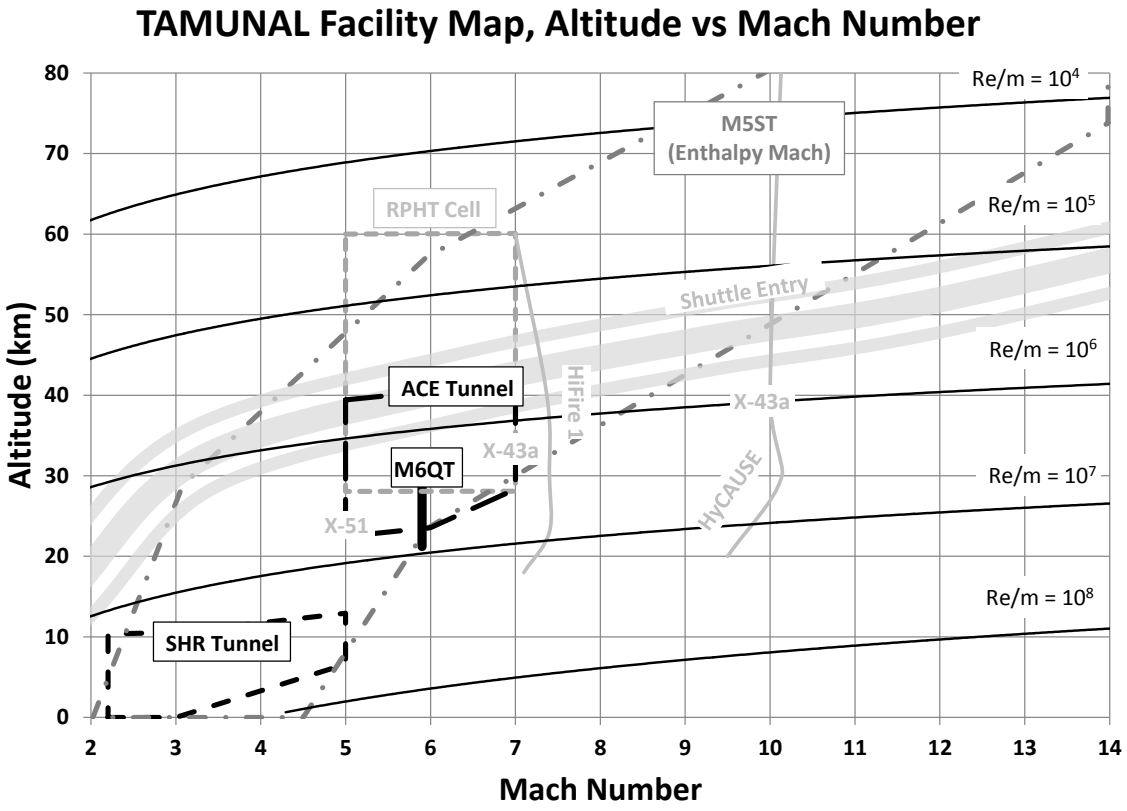

Figure 1.2: Flight Vehicle Trajectory Map, M vs. Altitude

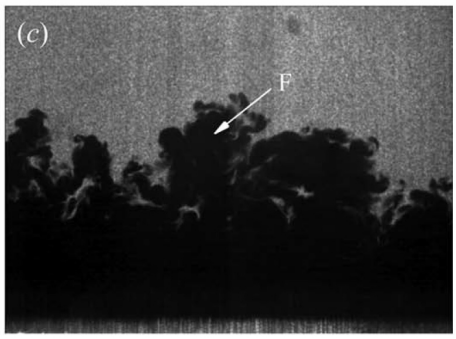

(a) Mach 4.9, $Re_\theta = 47000$ (Ref. 29)

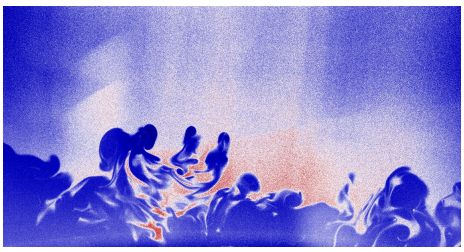

(b) Mach 5.6, $Re_\theta \approx 15000$

Figure 1.3: Comparison of Two Hypersonic Turbulent Boundary Layers

One of the most important questions asked when designing a flight vehicle is typically, "What is the state of the boundary layer?" It is well known that aerodynamic and thermodynamic characteristics change depending on the condition of the boundary layer. Knowing where a boundary layer transitions from its laminar state to the fully turbulent state is a very important and complex problem that has its own field of research dedicated to it. Equally important, however, is being able to predict the characteristics of a turbulent boundary layer for: heating concerns (providing adequate thermal protection or thermal inertia for preheating of fuel), flow stability and mixing (necessary to determine if the boundary layer will remain attached to the vehicle and if there is sufficient vorticity to mix air and fuel), and aerodynamic loads (knowing the skin friction of a vehicle to account for drag and also being able to properly size control surfaces). In the subsonic regime, there exist many models and computational solvers to predict these variables, mostly to an acceptable degree of accuracy. Additionally, wind tunnel or flight-testing can be performed on scale or full size models to validate preliminary estimates.

There have been many previous experiments conducted in the hypersonic flow regime in conventional blow-down tunnels, impulse (high enthalpy) facilities, and (to

a more limited extent) actual flight experiments. However, all of these facilities have limitations in regards to what they can achieve in terms of experimental similarity. Conventional facilities typically achieve Mach number similarity, but cannot achieve Reynolds number or enthalpy similarity (due to the nozzle expansion of the test gas). Impulse facilities can achieve Mach number and enthalpy similarity, but cannot test full-scale models. Flight-testing can of course achieve all the parameters experienced in normal flight, but testing full-scale models is prohibitively expensive and often times not practical for first order estimates. Because of these limitations and the limited number of suitable facilities, there exists a large scatter both in the quality of the data, and the availability. A survey of the available data from literature in graphic form is illustrated in Figure 1.4.

At the onset of hypersonic testing, focus was primarily on differences between the subsonic and supersonic regimes as compared to the hypersonic regime. To that extent, the experiments consisted of either qualitative information on complex bodies, or quantitative data on simple models. One of the earliest observed differences was the often inability of boundary layers to transition naturally from laminar to turbulent. This problem arose both from the stabilizing effect of higher Mach number flows, and the low Reynolds numbers typically found on sub-scale models. To combat the transition absence, the flow was artificially tripped using mechanical methods when the Reynolds number was found to be too low to promote natural transition. These naturally and forced transition boundary layers were the subject of extensive study and provided the basis for the next 20 years of theoretical speculation and empirical corrections for hypersonic flight.

In the more recent decades, the focus has shifted from characteristics of turbulent boundary layers, to studying roughness in an attempt to predict, control, and even create turbulent boundary layers. Several studies have sought to develop criteria

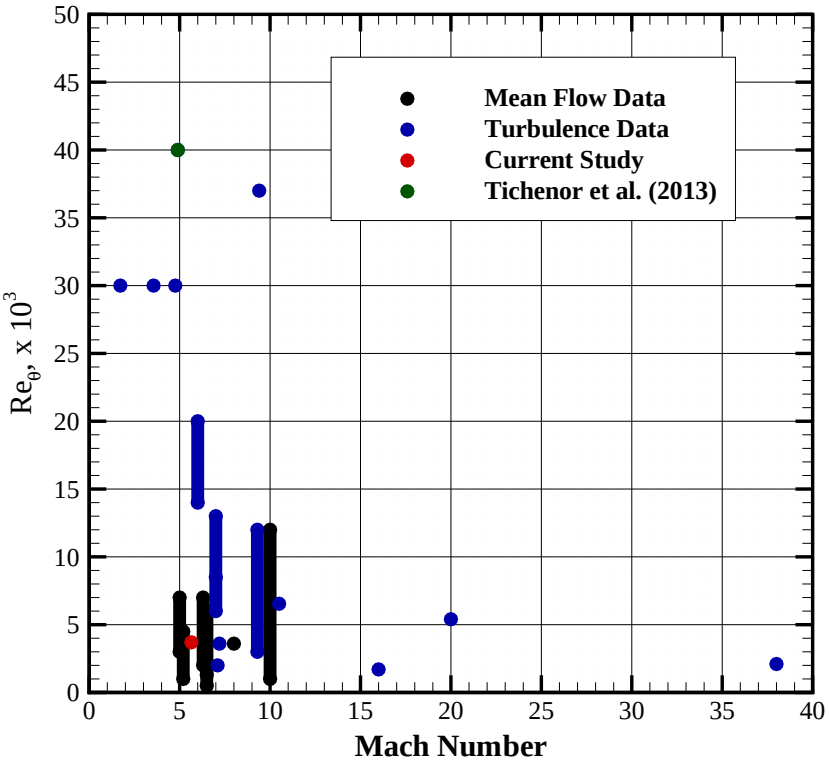

Figure 1.4: Summary of Available Hypersonic Data

for transition based on roughness characteristics, and other experiments have tried to manipulate flow using previous lessons regarding boundary layer tripping. The emphasis has shifted to what can be termed "trip sizing studies," and determining the effects of discrete or distributed roughness on a vehicle body.

A survey of previous literature and experiments has revealed two fundamental deficiencies in the data. First, the data exhibit large amounts of scatter, even under similar conditions and similar trip geometries. Second, there does not appear to be a significant amount of turbulence data (mean flow data is available at some conditions) at the high Mach, low Reynolds number spectrum of the list (see Figure 1.4). The objective of the current study is to address these two issues both in terms of technical contributions, and scientific contributions.

One of the main reasons for the lack of data in this region is the inherent difficulties in acquiring the data. The low Reynolds number aspect of the experiment typically translates to low densities and low pressures. As such, particle image velocimetry (PIV, a technique that tracks seeder particles in the flow) will often not work due to particle tracking issues. Even simple pressure measurements can become troublesome as the evacuation and equalization time of tubing can be quite long as compared to the facility run time. Low pressure and densities also create problems for surface measurement techniques such as pressure sensitive paint, temperature sensitive paint, and even simple oil flow topology. The hot-wire anemometry technique even requires adjustments as the wire is no longer subject to continuum flow in the low densities. As McGinley[45] et al. report, even some of the turbulence data available is subject to question due to poor frequency response and suspect calibrations.

The technical contributions of this study include:

1. the design and development of a low Reynolds number facility to conduct the current experiment,

2. the design and development of instrumentation necessary to collect data at these challenging flow conditions,

3. and the collection of high-quality, archival data useful for future comparisons to similar experiments, or high fidelity LES and DNS simulations.

From a scientific perspective, the questions this study will seek to answer are:

1. Do current scaling laws (Morkovin and Van Driest) hold in this hypersonic, low Reynolds number regime?

2. Are 2-dimensional simulations sufficient for tripped boundary layers, or are 3-dimensional simulations inherently necessary?

3. Does the turbulent power spectra (when properly scaled) adhere to traditional power law comparison?

4. Do the effects of this low Reynolds number, hypersonic regime modify the near-wall turbulence properties?

5. How do the boundary layer disturbances change (growth rates) downstream of the trip?

2. BACKGROUND AND LITERATURE REVIEW

In this chapter, the basic theory behind boundary layers and turbulence properties will be highlighted, followed by a review of the literature and available data. Building on this review, the need for additional experimental data at specific conditions will be addressed, concluding with the goals of the current study as it pertains to the overarching objective of hypersonic research.

2.1 Boundary Layer Theory

As a fluid flows over a surface, there is a thin region near the surface formed known as the "boundary layer." This boundary layer exists due to viscosity which necessitates boundary conditions at the fluid-surface interface, and the freestream interface. These conditions are most often "no slip" at the surface, and a velocity approaching the freestream at the boundary layer edge (not always the case though for low density situations or shear layers). Despite the limited region this boundary layer influences, it is directly responsible for many aerodynamic properties including lift, drag, and heat transfer. Therefore, accurately predicting the boundary layer in terms of size, stability, and state (laminar or turbulent) is of the utmost importance when discussing vehicle design and analysis.

The basic laws of conservation of mass, momentum, and energy (as derived in White[77]) can be expressed as,

$$\frac{\partial \rho}{\partial t} + \nabla \cdot \rho \mathbf{V} = 0 \tag{2.1a}$$

$$\rho \frac{D\mathbf{V}}{Dt} = \rho \mathbf{g} + \nabla \cdot \tau'_{ij} - \nabla p \tag{2.1b}$$

$$\rho \frac{Dh}{Dt} = \frac{Dp}{Dt} + \nabla \cdot (k \nabla T) + \tau'_{ij} \frac{\partial u_i}{\partial x_j} \tag{2.1c}$$

$$\tau'_{ij} = \mu \left(\frac{\partial ui}{\partial x_j} + \frac{\partial u_j}{\partial x_i} \right) + \delta_{ij} \lambda \nabla \cdot \mathbf{V} \tag{2.1d}$$

Following the basic assumptions for boundary layer flow, and neglecting buoyancy, the continuity and momentum equations for steady flow are,

$$\frac{\partial u}{\partial x} + \frac{\partial v}{\partial y} = 0 \tag{2.2a}$$

$$u \frac{\partial u}{\partial x} + v \frac{\partial u}{\partial y} = U \frac{dU}{dx} + \nu \frac{\partial^2 u}{\partial y^2} \tag{2.2b}$$

$$u(x,0) = v(x,0) = 0 \qquad u(x,\mathrm{inf}) = U(x)$$

These sets of equations are applicable to laminar, incompressible boundary layers. In Morkovin's[52] 1962 paper, he surmised that "the essential dynamics of compressible shear flows will follow the incompressible patterns". Therefore, as long as Mach number fluctuations are much less than unity, the fluctuations in density and enthalphy will not modify the turbulence structure significantly. Using this basic hypothesis, the previous set of equations can be modified to account for compressibility. Furthermore, following the work of Van Driest[73], the equations can be averaged to give,

$$\frac{\partial}{\partial x}\left(\overline{\rho u}\right) + \frac{\partial}{\partial y}\left(\overline{\rho v}\right) = 0 \tag{2.3a}$$

$$\overline{\rho u}\frac{\partial \overline{u}}{\partial x} + \overline{\rho v}\frac{\partial \overline{u}}{\partial y} = \rho_e U_e \frac{dU_e}{dx} + \frac{\partial \tau}{\partial y} \tag{2.3b}$$

$$\frac{\partial \overline{p}}{\partial y} = -\frac{\partial}{\partial y}\left(\overline{\rho v' v'}\right) \tag{2.3c}$$

$$\tau = \overline{\mu}\frac{\partial \overline{u}}{\partial y} - \overline{\rho u' v'}.$$

The above equations form the basis for the starting point of turbulence models.

At this point, it becomes instructive to define the nature of turbulence. As detailed by Cebeci[14] et al., the following three statements adequately define the subject.

> Turbulence is an irregular motion which in general makes its appearance in fluids, gaseous or liquid, when they flow past solid surfaces or even when neighboring streams of the same fluid flow past or over one another. -von Kármán[74]

> Turbulent fluid motion is an irregular condition of flow in which the various quantities show a random variation with time and space coordinates, so that statistically distinct average values can be discerned. -Hinze[27]

> ...turbulence has a wide range of wave lengths. -Bradshaw[12]

2.2 Turbulence Closure and Modeling Limitations

At the heart of these equations lies what is referred to as "the closure problem of turbulence." To solve this system of equations, additional constituent relations are required. Specifically, equations of state for the fluid (thermal, caloric, viscosity, etc.),

and an equation to describe the turbulent shear stress term. Not shown here is the energy equation, which is similar in nature to the momentum equation. The energy equation contains its own new term, known as the turbulent heat flux, which also requires a model for closure. The models used to describe the turbulent shear stress have been the subject to extensive research, and range from simple algebraic models, multiple equation models, and full differential equations of evolution models. In the end, however, the goal of any model created is ultimately to reproduce experimental data.

As Morkovin[51] et al. discuss, there are many different mechanisms which can lead to boundary layer transition. The intensity of the initial disturbance level can alter the paths to transition, and if this intensity is sufficient enough, some parts may be bypassed or not exist at all. Boundary layer transition is indeed a complex matter, and has its own dedicated field of research and modeling associated with it. Natural transition is often modeled with a set of parabolized stability equations, but there remains a question of how to properly model transition from a singluar or array or roughness trips. In many DNS and LES simulations, the "trip" used to create a turbulent boundary layer can vary between inflow perturbations, mass flux additions, or fluctuating flow properties at the trip location.

Understanding the flow physics created by a physical trip, as well as the structure of the tripped boundary layer is important not only for an improved understanding of the processes, but also for numerical simulations that add "inflow perturbations" to artificially trip the flow. Subbareddy[69] et al. used dual pairs of counter-rotating streamwise vortices that create a sequence of "downwash" and "upwash" events in the boundary layer as the inflow disturbance mechanism. These perturbations are similar in nature to the disturbances created by the trips used in this experiment.

Bathel[4] et al. remark that currently no general method exists which is capable of consistently computing even the most basic of transition parameters, the transition location, over a range of hypersonic flow conditions. And while CFD tools are currently being designed to capture flow physics, the simple geometries being simulated need high-quality data sets for comparisons.

In a world where computing power is ever increasing, a frequent question arises, "Why is experimental data still necessary with computational capability approaching direct numerical simulation (DNS) of real-world flows?" As Schlatter[61] et al. point out, data from "numerical experiment" turbulent boundary layers should be viewed with the same scrutiny as experimental data. As the authors point out, most of the variations in data from DNS boundary layers can be attributed to the differences in tripping conditions. As such, DNS is not an incorruptible technique, and experimental data is still required to improve its accuracy and validate its results.

Tennekes[70] et al. argue that the ratio of the largest scales to the smallest scales of a fluid scales with $Re^{3/4}$. Therefore, an increase in Reynolds number will always result in a decrease in the relative scale of the smallest observable coherent structures in the boundary layer (because the largest structures scale with δ). Because a direct numerical simulation must solve for all relevant flow scales (and time scales), increasing Reynolds number significantly increases the amount of flow scales (and therefore the resolution of the grid) that must be computed.

While current progress is being made towards the evolution of LES and DNS codes, Subbareddy[69] et al. note that RANS models have received little effort in an attempt to improve their results for highly compressible flows. These codes were originally developed for incompressible or weakly compressible flows, and typically the only modification made when considering highly compressible flows is a simple compressibility correction.

2.3 A Lack of Experimental Data

As was discussed in Chapter 1, there are situations where having a turbulent boundary layer is necessary to achieve desirable performance. As Berry[7] et al. point out, turbulent boundary layers increase inlet operability and enhance overall engine performance. Unfortunately, there exist very little data regarding forced transition in ground facilities, and the number of flight data in existence is even less. The entire purpose of the research done by Berry et al. was necessitated by the lack of confidence in numerical methods to properly predict transition caused by an array of roughness elements. And while the research was very effective in sizing trips based on transition location, there were no data taken pertaining to the structure and characteristics of the turbulent forced boundary layer itself.

A common concern for using ground based facility data is the inherent "tunnel noise" present in such facilities that is not found in the quiescent atmosphere. Previous research has shown a strong correlation between noise levels found in conventional facilities and transition prediction. Borg[10] et al. found that tunnel noise had a substantial effect on roughness-induced transition. Some studies have shown that not only are noise levels less of a factor in the hypersonic regime, but that standard acoustic disturbances found in these facilities are often at much lower frequencies than those required to excite dominant hypersonic instabilities[34,56,68]. Nevertheless, data from ground facilities and from flight testing still display a large disparity in natural transition Reynolds number. While this problem is of significant importance when discussing transition location and mechanisms, the study of turbulent boundary layer structure and characteristics is not as susceptible to "tunnel noise."

Despite the importance of an experimental database of hypersonic turbulent boundary layer data, McGinley et al. point out there exists a dearth of quality

data that can be used to validate computational counterpart experiments. A list of available data found in the literature from References 22, 23 and 45 has been compiled in Tables 2.1 and 2.2. Table 2.1 contains a list of experiments that acquired mean flow data (pressure, temperature, and in some cases, skin friction) for a variety of conditions, and Table 2.2 contains a list of data available with turbulence quantities measured (either through hot-wire, electron beam, LDV, or PIV). A note worth making regarding available experiment data: the data exhibit large amounts of scatter, even among experiments with similar conditions. These differences can be attributed to differences in facilities, experimental setups, or even measurements locations. Therefore, when comparing experimental data to computational data, it is worth investigating the conditions under which the experimental data was collected. This inherent scatter was one of the reasons spanwise measurements were also selected for the current campaign. Providing some indication of the spanwise uniformity of the flowfield will aid others in repeating, simulating, or comparing data to the current experiment.

Table 2.1: Available Mean Experimental Data

Authors	Mach Number	Re_θ	Wall Temp.	Type	Measurements
Baumgartner[5]	8	3600	Cold	ZPG	Pitot & temperature
Danberg[17]	5.1	3000-4000	0.8-0.9	ZPG	Pitot, temperature & force balance
Danberg[18]	6.5	13000-6000	0.5-0.9	ZPG	Pitot & temperature
Fischer et al.[24]	6.5	500-6000	1.0	Wedge	Pressure
Keener et al.[31]	6.3	2000-7000	0.3-0.5	ZPG	Pitot, temperature, & force balance
Lee et al.[42]	5	4800-56000	0.5-1.0	ZPG	Pitot & temperature
Moore[50]	5	3000-7000	0.5-1.0	ZPG	Pitot
Watson et al.[75]	10	1000-12000	1.0	ZPG	Pitot, temperature, and force balance
Winkler et al.[80]	5.2	1000-4500	0.6-1.0	ZPG	Pitot & temperature

Table 2.2: Available Turbulence Experimental Data

Authors	Mach	Re_θ	Wall Temp.	Type	Measurements
Bartlett et al.[3]	9.3	3000-12000	0.3	ZPG	Pitot, temperature & electron beam
Berg[6]	6	14000-20000	0.9	ZPG	Pitot, temperature & hot-wire
Fischer et al.[25,26]	20	5400	Adiabatic	Nozzle	Hot-wire
Kemp et al.[33]	38	2100	Cold	Nozzle	Hot-wire
Kistler[35]	1.72, 3.56, 4.67	30000	-	ZPG	Hot-wire
Laderman[38]	7.1	2000	Cold/Adiabatic	ZPG	Hot-wire
Laderman et al.[19,39,40]	9.4	37000	Cold	ZPG	Hot-wire
Materna[44]	16	-	Adiabatic	Nozzle	Hot-wire
McGinley et al.[45]	10.5	6540	-	Wedge	Hot-wire
Mikulla et al.[47,48,49]	7	8500	Cold	ZPG, APG, SWBLI	Wire on ceramic
Owen[53]	6	-	-	ZPG, APG	LDV
Owen et al.[54,55]	7	6000-13000	Cold	ZPG	Hot-wire
Sahoo et al.[60]	7.2	3600	-	SBLI	PIV
Semper	5.7	3700	Adiabatic	ZPG	Pitot, temperature, & hot-wire
Smith et al.[65]	16	1700	Adiabatic	Tunnel wall	Electron beam
Tichenor[72]	4.9	40000	0.9	Tunnel wall	PIV
Williams et al.[79]	7.4	-	0.73	ZPG	PIV

2.4 Hypersonic Flows

As McGinley[45] et al. cite, turbulence plays a significant role in the following flow phenomena:

1. Separated and vortical flows,
2. Control-surface flows,
3. Shock-wave/boundary-layer interactions,
4. Transition prediction,
5. Low-loss fuel/air mixing,
6. Shock/shock interactions,
7. Boundary-layer ingestion.

The authors go on to discuss (and as was highlighted in the previous section) that despite the importance of these complex flows, there is a lack of even the simple flat plate, zero pressure gradient data.

Commonly, experiments are performed at moderate to high Reynolds numbers for ease of data acquisition, while DNS simulations are performed at low Reynolds numbers for computational accessibility. However, comparing these low Reynolds number DNS simulations to high Reynolds number experimental data will inevitably lead to incorrect conclusions[9,58,59].

As Kistler[35] points out (and as was discussed previously), much of the past research into turbulent boundary layers (analytical and experimental) has focused on mean flow properties, such as skin-friction coefficient, heat-transfer coefficient, and

velocity field. The structure of the turbulent field itself is equally important in order to understand why the above quantities vary as they do.

Hypersonic vehicles experience a different set of flow phenomena (see Figure 1.1) than subsonic or supersonic vehicles. As such, it is very likely to expect a hypersonic boundary layer to be inherently different than the boundary layer of the lower speed regimes. Of the flow phenomena present in Figure 1.1, the one most prominent in the current experiment is viscous interaction. Hypersonic boundary layers grow more rapidly than at slower speeds, and the extreme thickness of the boundary layer flow can cause the outer invisid flow to change greatly as well[2]. The outer inviscid layer interaction with the boundary layer is termed *viscous interaction.*

Extreme viscous dissipation near the wall, increased importance of pressure fluctuations, the probability of supersonic relative velocities between organized motions and high-speed entrained fluid, and the nature of transition are all factors which can contribute to differences in the boundary layer[45]. McGinely et al. postulate that the mean flow properties can be significantly affected by the sharp temperature gradients across the boundary layer due to the large viscous dissipation rates. In turn, these mean-property variations can cause significant density fluctuations which create a region near the wall where low Reynolds number effects become especially important. Kovásznay[37] found that the fluctuation field in supersonic boundary layers appeared to be similar to low speed boundary layers, with the primary difference being the increased intensity of temperature fluctuations due to the increased turbulent heat transfer.

In addition to the effects of compressibilty and low-Reynolds number, the tripping device selected will also influence the turbulence structure. Williams[79] et al. note that the curved shock pattern created by a trip will generate additional vorticity (a major effect of the current trip) that can modify turbulence statistics. Understanding

these effects at high speeds is necessary to gauge the effectiveness of scaling techniques such as those given by Morkovin and Van Driest.

Kovásznay and Morkovin both came to a similar conclusion that as long as the Mach number fluctuations are small in a boundary layer, the dynamics of the compressible turbulent boundary layer should mimic those of the incompressible turbulent boundary layer[37,52]. However, since hypersonic boundary layers can posses large values of fluctuating Mach number, more research is needed to determine how these fluctuations affect the basic characteristics of the boundary layer[40,54].

2.5 Current Study

Cheng[15] describes the current bifurcation of hypersonics research into transition and compressible turbulence experiments, and the study of free-molecular flows. The current study was created to address the former by answering some of the questions outlined above, as well as to fill a niche in the available data. By probing a turbulent boundary layer with an Re_θ value of only 3700, the experimental campaign can readily be simulated using LES or DNS solvers.

It is the hope of the author that the data acquired here can be used both to validate numerical solving capability at low Reynolds numbers, and potentially identify any discrepancies between the trip used in this experiment, and the numerical "trips" used in computational studies. By probing several location downstream of the trip, the growth rates of boundary layer disturbances can also be examined.

While the current study may not fully answer all of the questions regarding hypersonic, low Reynolds number turbulent boundary layers, it is nevertheless an important stepping stone. The facility created here, in conjunction with the instrumentation developed for the project allow for future studies to acquire additional data or probe additional flow conditions or geometries.

3. EXPERIMENTAL SETUP

This chapter details the research facility designed, built, and utilized for the current study, the model geometry selected for investigation, the instrumentation used to acquire the data, and the processing techniques used to analyze the results.

3.1 The ACE Facility

The Actively Controlled Expansion (ACE) Hypersonic Tunnel is a unique, variable Mach number facility housed within the Texas A&M University National Aerothermochemistry Laboratory (TAMU-NAL). This facility utilizes a variable Mach number mechanism that can be operated both statically between tests, and dynamically as the tunnel is running. The long duration run time of the facility (up to 50 seconds) allows for usage of modern laser techniques (PIV, PLIF, MTV, & VENOM) along with conventional diagnostics (pressure, temperature measurement, hot-wire) to provide basic quantitative turbulence flow statistics for aerodynamic/aerothermal investigation, model development and validation. The low density, low Reynolds number environment created by the expansion nozzle also permits data to be collected in a challenging flow regime for experimental research. The ACE tunnel has proven reliable and repeatable, where to date, over 1000 runs of the facility have been logged at various Mach numbers. Flow uniformity and freestream turbulence levels were examined previously[62,63,71].

The facility in its entirety consists of (1) a uniquely designed settling chamber, (2) an actively controlled expansion nozzle, (3) a test section, (4) an adjustable diffuser and (5) the necessary infrastructure to drive the facility. The nozzle design methodology consisted of a combination of classical methods and high fidelity computational fluid dynamics (acknowledgments to Dr. Ravi Srnivasan for his computational ef-

Table 3.1: ACE Wind Tunnel Operating Conditions

Mach No.	P_{t1} (kPa)	T_{t1} (K)	Run Time (sec)	Test Section (m)
5 - 7[1]	48 - 900[2]	290 - 460[2]	50	0.23 x 0.36

forts). A complete description of the design, including recent modifications and calibration experiments can be found in References 62, 63 and 71.

The ACE hypersonic wind tunnel operates in an open-circuit, blow-down, pressure-vacuum mode. The available flow conditions are summarized in Table 3.1. The major components of the ACE tunnel are shown in Figure 3.1 and include the settling chamber, planar nozzle, test section, and diffuser.

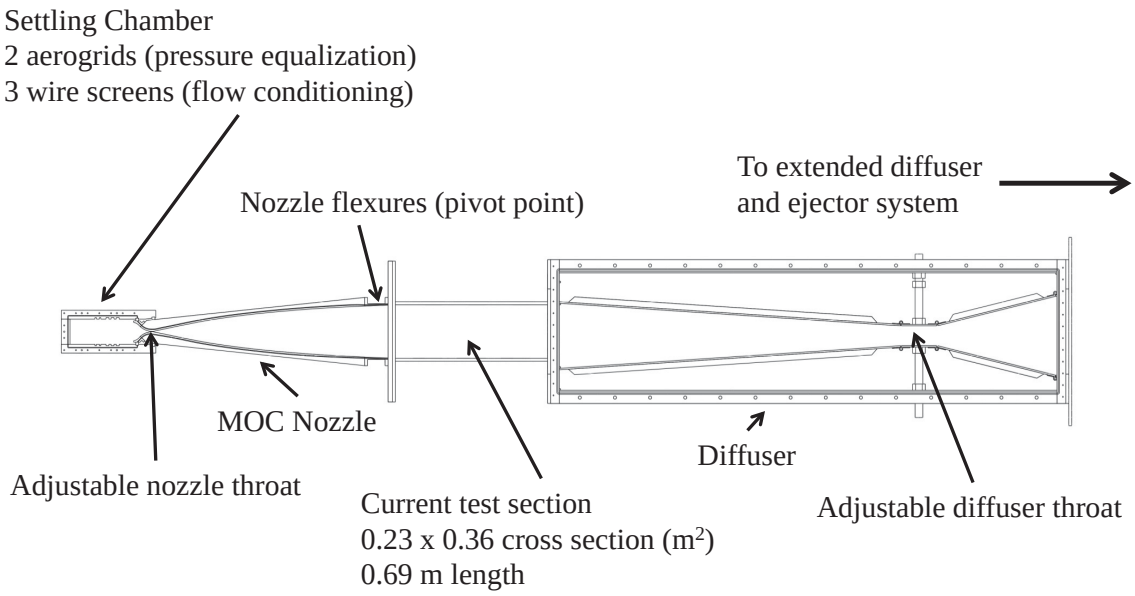

Figure 3.1: Schematic of the ACE Wind Tunnel Flow Path

[1]Studies on the upper Mach number limit for the facility are planned pending improvements in the heating infrastructure

[2]Improvements to the infrastructure will increase the maximum pressure to $1380kPa$ and the maximum temperature to $533K$

3.1.1 Settling Chamber

The settling chamber is a stainless steel rectangular pressure vessel that slips over the nozzle extension lips. The current design was revised from Reference 71 to include a new sealing mechanism which allows Mach number variation without requiring re-positioning of the entire chamber. The new silicone rubber seal designed for this purpose, and the nozzle extension lips are shown in Figure 3.2a. Heated air is delivered to the settling chamber through a manifold of four airlines connected to the rear of the chamber. The air first passes through a series of two aero-grids with approximately 700 holes at $3.2mm$ diameter, and then three wire meshes of decreasing porosity to reduce flow turbulence and angularity before entering into the converging section of the nozzle (Figure 3.2b).

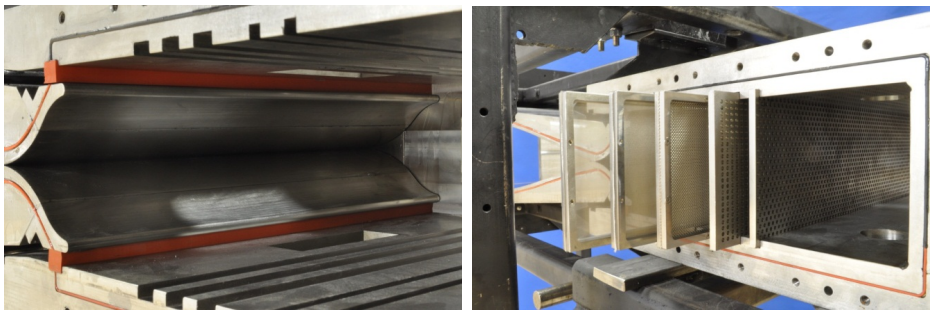

(a) Nozzle Throat with Flexible Seal (b) Aerogrids and Screens

Figure 3.2: ACE Settling Chamber Seals & Flow Conditioning

The most notable feature of the ACE tunnel is its continuously variable Mach number, which is achieved by rotation of the method of characteristics designed nozzle planes about the nozzle exit via the custom designed flexures. This design necessitates moving seals between the nozzle planes and the sidewalls, and the nozzle throat and settling chamber. The nozzle planes were designed to float between the

sidewalls with O-ring seals, where the planes are separated from the sidewalls by the allowable O-ring gap ($0.13mm$). The flexible rubber seal, shown in Figure 3.2a, allows free movement of the planes at their termination point in the settling chamber. The nozzle contraction, shown in Figure 3.3, starts with a large lip and is relatively short, which results in boundary layers with an abbreviated development length before entering the throat region of the nozzle. Facilities designed for quiet flow (low disturbance), on the other hand, typically have large contraction ratios (contraction inlet area to throat area ratio) to reduce incoming flow disturbances.

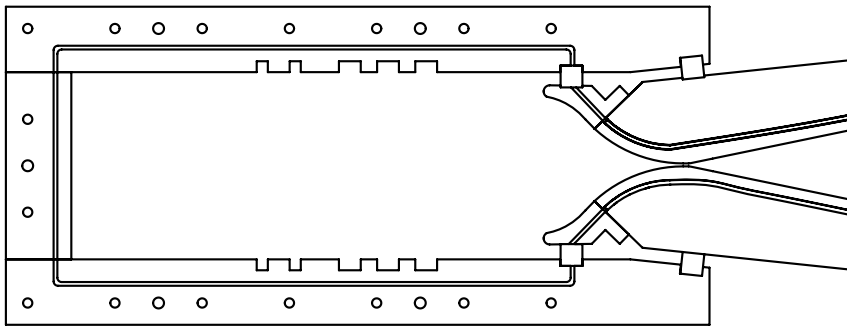

Figure 3.3: Settling Chamber and Nozzle Interface Internal View

3.1.2 ACE Supersonic Nozzle

The supersonic portion of the ACE nozzle was designed using a combination of method of characteristics (custom program written by Dr. Bowersox) with viscous corrections, and full three-dimensional computational fluid dynamics (CFD). The characteristic mesh consisted of 100 characteristics with a total of eight expansion fans, including the final wave cancellation. The dark half diamond structure near the throat in Figure 3.4 shows the intersection points of the characteristic lines, and

the dashed line shows the estimated boundary layer thickness[73]. As indicated, the maximum core flow region was at x = 1.02m, hence, the nozzle was truncated at this location. The method of characteristics design was centered around the Mach 7 flow condition. Rotation of the nozzle planes about the nozzle exit resulted in small errors in the initial wall angle for Mach numbers as low as 5. The upper Mach number is limited by the viscous boundary layer growth, which increases with Mach number. Flow uniformity and stability has been tested up to Mach 7, and future tests may see the facility's quoted limit increased to Mach 8.

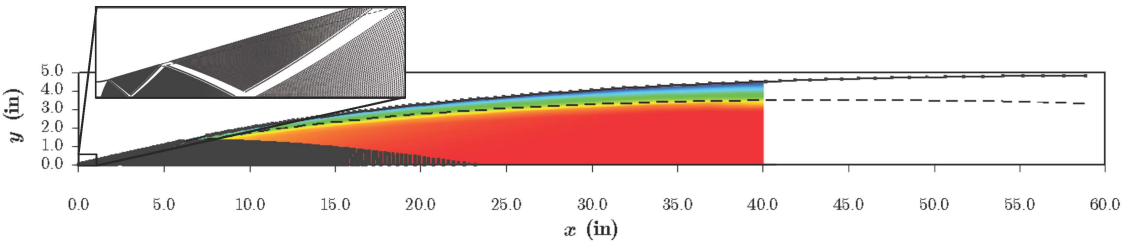

Figure 3.4: Method of Characteristics Nozzle Design Results (M = 7)

The nozzle flowfield was computed with the GASP[1] flow solver using both parabolic and elliptic methods. Turbulence effects were simulated using the one-equation model, two-equation models, and Wilcox's Reynolds stress-ω transport model[46,66,78]. Sample results for the Mach 5 and 7 conditions are shown in Figures 3.5a - 3.5c. The color contours on the exit plane are those of Mach number, while the grey scale contours in the lateral and transverse cross-sectional plane show contours of density gradient. Mach number profiles on the exit plane in both directions of symmetry are illustrated by the line plots. The comprehensive CFD results confirmed the initial nozzle design. The finished nozzle with attached settling chamber is shown in Figure 3.6.

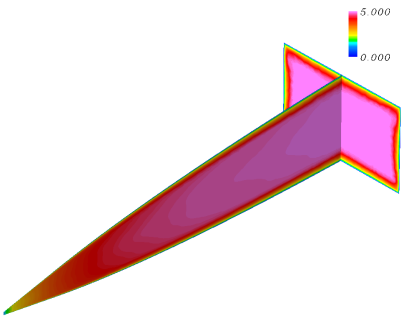

(a) Mach 5 Contours

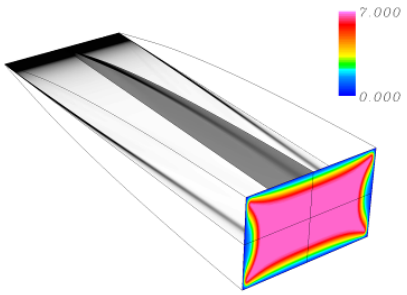

(b) Mach 7 Contours

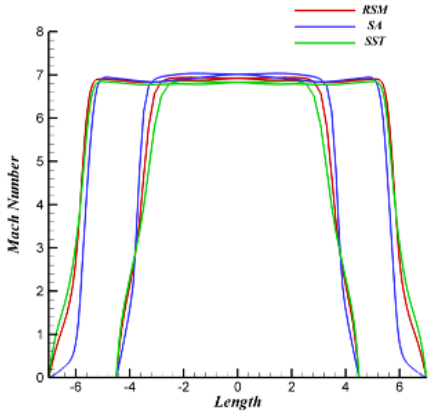

(c) Mach 7 Exit Profile

Figure 3.5: ACE CFD Results

3.1.3 Test Section

The test section utilized for the current study was $0.69m$ long with parallel walls containing three access ports incorporated into each surface of the test section at $0.15m$, $0.34m$, and $0.53m$ from the nozzle exit; see Figure 3.7. These ports allowed for the installation of $150mm$ windows for optical access, or different instrumentation configurations.

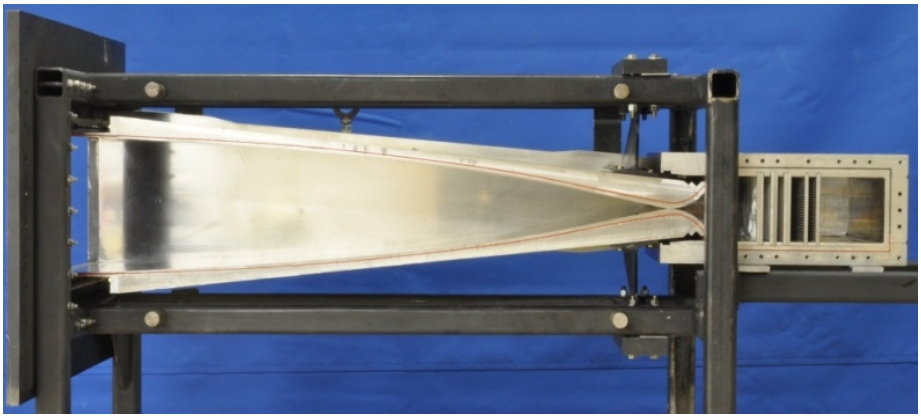

Figure 3.6: ACE Nozzle and Settling Chamber

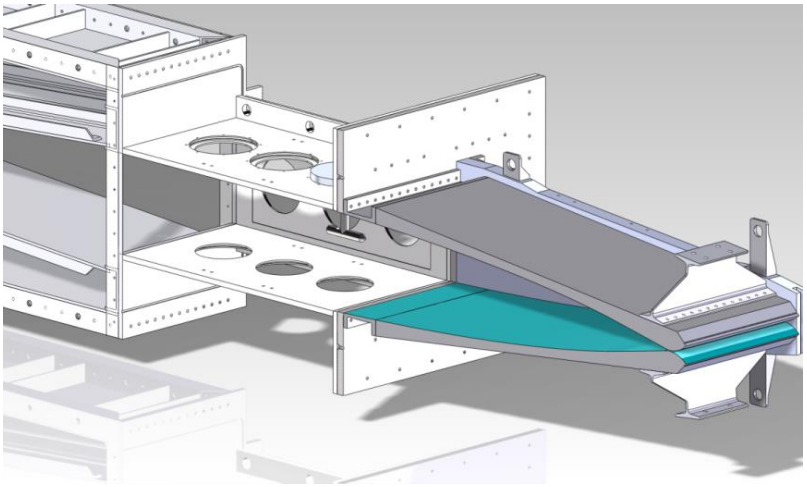

Figure 3.7: ACE Tunnel with Current Test Section

3.1.4 Diffuser

The diffuser was designed following Wegener[76] and Bertram[8], with the geometry chosen to match Bertram. For optimum efficiency, a supersonic diffuser is recommended to have a convergence section long enough to contain at least two oblique wave reflections before the diffuser throat. The diffuser throat height is selected to balance the conservation of mass through the nozzle throat, and to optimize the op-

erating conditions. As the throat height is adjusted, the upstream convergence angle changes. The throat height can be adjusted continuously from $0.10m$ to $0.23m$, where the throat geometry allows the upper and lower surfaces to be symmetric up to the diffuser throat. To quantify diffuser performance, a pitot pressure probe was used to monitor the supply pressure in the settling chamber, and a static pressure port was used to measure the pressure at the diffuser exit. By comparing pressure data at both locations at various Mach numbers, the required pressure ratios to start and run the tunnel were experimentally determined. The diffuser efficiency (defined here as the diffuser pressure divided by the theoretical pressure behind a normal shock at the diffuser throat) was experimentally determined to be approximately 0.7 - 0.8 depending on Mach number.

3.1.5 Infrastructure

The infrastructure includes two $16.2MPa$ ($2350PSIG$) air compressors[1] (14.2 standard m^3/min) and a $23.2m^3$ storage tank. This system provides filtered (99% efficient submicron), dry ($233K$ dewpoint) air. A $0.5MW$ Chromalox brand heater is available to preheat the air supplied to the tunnel to $533K$ (Currently, temperature variations can be as much as $20K$ during a run. Future improvements will attempt to lessen this drift). Tunnel supply pressure is controlled through a series of 2 Stra-Val pressure regulators (the settling chamber pressure typically drifts by $200kPa$ or less during a run). A Fox brand two-stage air ejector is used to provide the vacuum side to the hypersonic wind tunnel. This ejector system requires approximately $21kg/s$ at nominally $1.1MPa$, which is the limiting factor in the 50 second facility run time.

[1]These compressors have since been retired in favor of more modern replacements

3.1.6 Performance and Flow Quality

Pressure in the settling chamber is measured with an Endevco 8540-200 (0-1379kPa full scale) piezoresistive transducer. The Mach numbers at the nozzle exit and in the test section are monitored by a static pressure port and a pitot probe respectively. The nozzle static port is a 3.18mm hole located approximately 0.15m upstream of the nozzle exit. The static pressure is measured by an MKS Baratron 631C capacitance manometer (0-1333Pa range) that is internally heated to 473K with no appreciable drift in zero or linearity at high temperatures. The pitot probe is connected to an identical Baratron transducer (0-13.3kPa range) outside of the test section. More detailed information on the instrumentation used for the freestream characterization campaign is available in Reference 62. Diffuser pressure is monitored with an MKS 902 sensor (0-106kPa full scale). Temperature in the settling chamber is monitored with an exposed end, type-K thermocouple.

3.1.6.1 Tunnel Performance Curves

The performance maps for the facility as determined experimentally are shown in Figure 3.8. The solid curves correspond to the available pressure ratio based on the measured ejector performance, and the dashed lines correspond to the requirements for operation at a 75% diffuser efficiency. Also shown are light dashed lines of constant tunnel static pressures (in Pa). At the higher Mach numbers, liquefaction becomes important, and is determined by both the static temperature and static pressure in the test section. The double lines denote the liquefaction limits (liquefaction was determined following Pope[57]), where liquefaction occurs to the right of the double lines. The black lines correspond to liquefaction limitations in the current configuration, where losses in the system limit the upper temperature in the settling chamber to 460K. The light gray lines denote the potential increases in tunnel

performance when operation at full temperature ($533K$) is achieved. Figure 3.9 is a comparison of the ACE facility and other available facilities at the TAMU-NAL site, and also depicts actual flight vehicle trajectories in relation to facility operating limits.

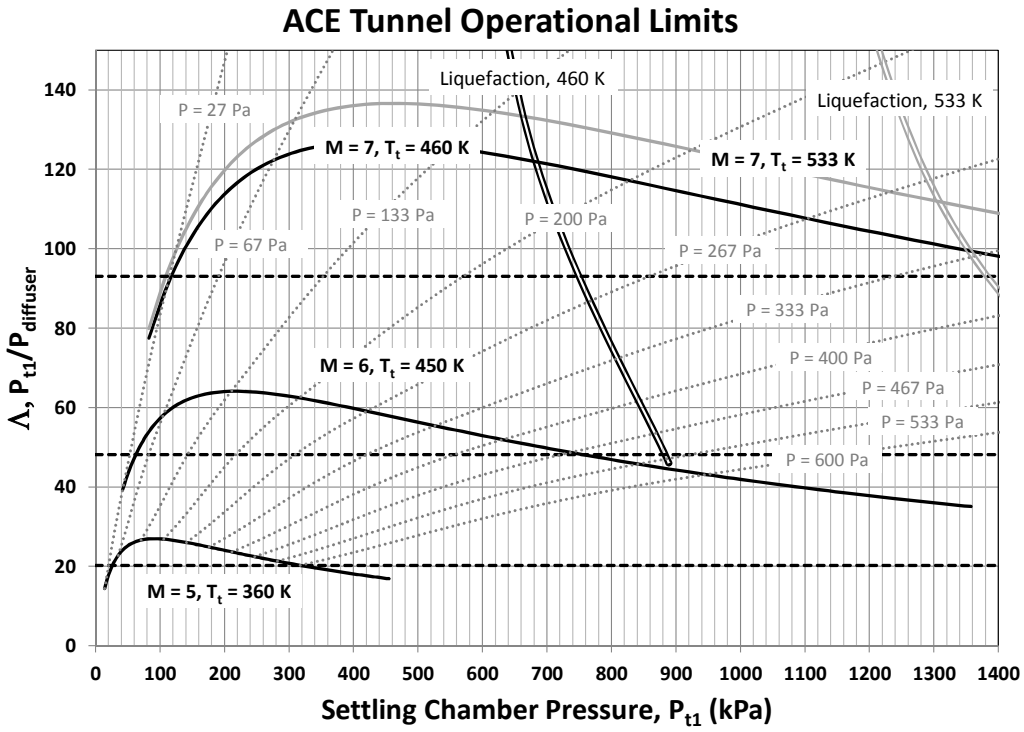

Figure 3.8: ACE Performance Curves

3.1.6.2 Freestream Flow Quality

Freestream turbulence level results for Mach 5, 6, and 7 over a range of unit Reynolds numbers are presented here. For more information on the experimental determination of the freestream quality, see Reference 62.

The ACE tunnel root-mean-square pressure fluctuations were computed and are compared to other tunnels in Figure 3.10. The present values are significantly lower

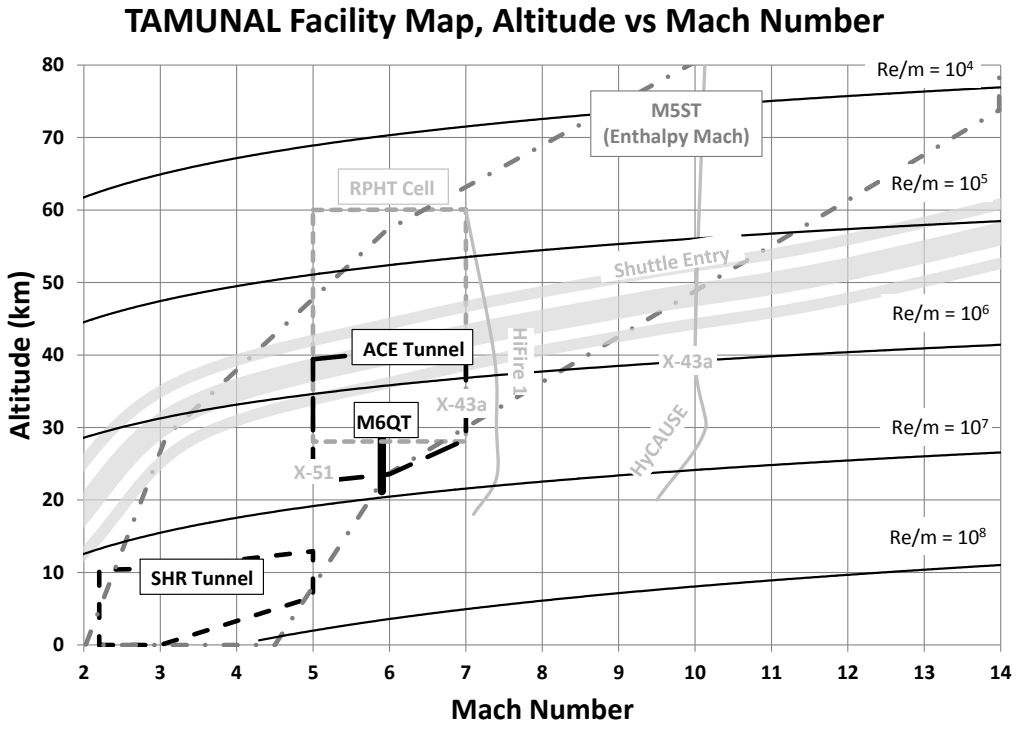

Figure 3.9: ACE Mach Number versus Altitude Map

than those found in most conventional facilities. While the comparison in Figure 3.10 presents an interesting (and somewhat biased) view of tunnel noise in various facilities, the raw numbers do not include corrections for facility size or Mach number. Figure 3.11 provides a more weighted comparison of the facilities by scaling the tunnel noise by dynamic pressure and the freestream unit Reynolds number by nozzle exit diameter[41].

The most recently acquired uniformity data acquired (shown in Figure 3.12) at Mach 6 shows the RMS Mach number variation across the exit plane to be less than 0.5% of the exit Mach number[62].

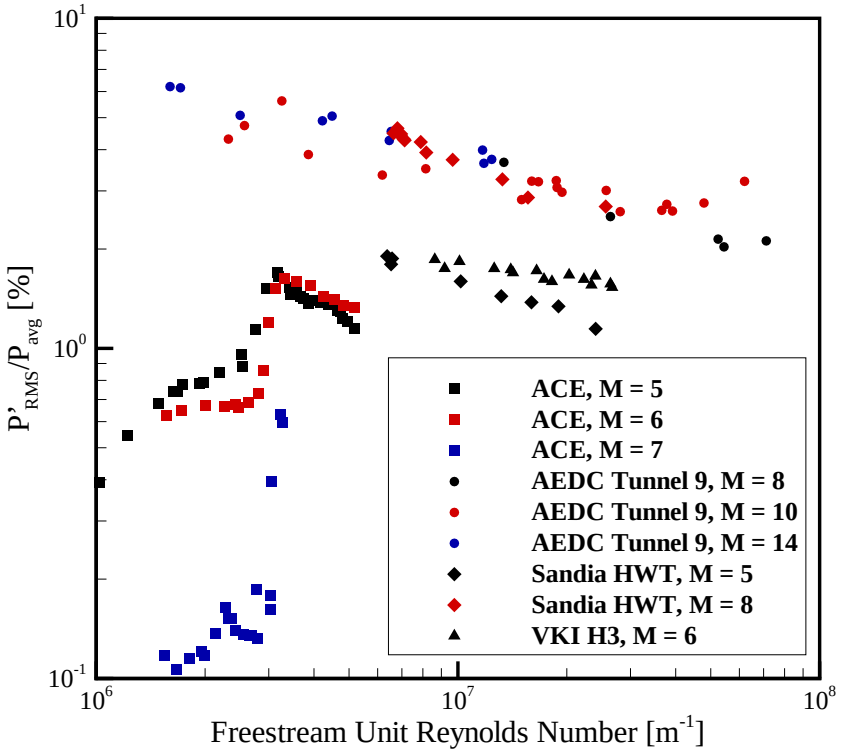

Figure 3.10: ACE Freestream Fluctuations Compared to Other Facilities

3.2 Model Design

To address the questions posed in Chapter 1, it was necessary to fabricate a model to test in the above-described facility. A review of the literature and knowledge of data acquisition techniques led to the design of an aluminum flat plate model with an array of trips at the leading edge to promote laminar-turbulent transition of the boundary layer. The model and its associated trip design are discussed in this section.

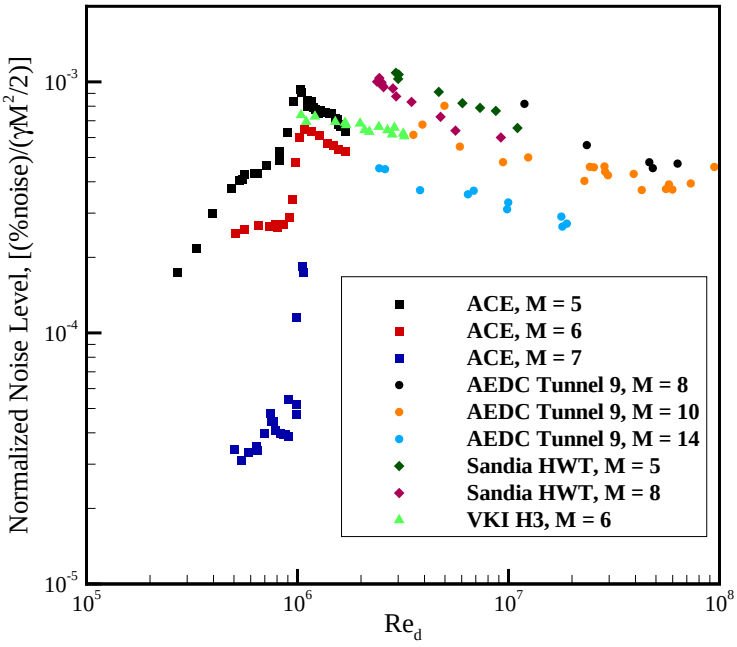

Figure 3.11: Scaled Freestream Fluctuations

3.2.1 Flat Plate

For the current set of experiments, a flat plate model was designed and manufactured (Figure 3.13). The plate was approximately 508mm long and 7.62mm thick with a 1.59mm radius blunt leading edge, and extended nearly the span of the tunnel at 355.6mm wide (with a 1.59mm gap on either side to allow for easier mounting in the tunnel). A 10° ramp on the underside of the model extended 43.88mm from the leading edge to the point at which the thickness became 7.62mm. The model was mounted via struts on the underside of the plate, leaving the topside (measurement side) free of any hardware that may have introduced Mach waves or other disturbances. The leading edge of the model was positioned along the vertical centerline of the tunnel ($y_{absolute} = 115.89mm$) at a 2° downward angle of attack. The slight angle of attack was chosen to promote a stagnation point on the top surface

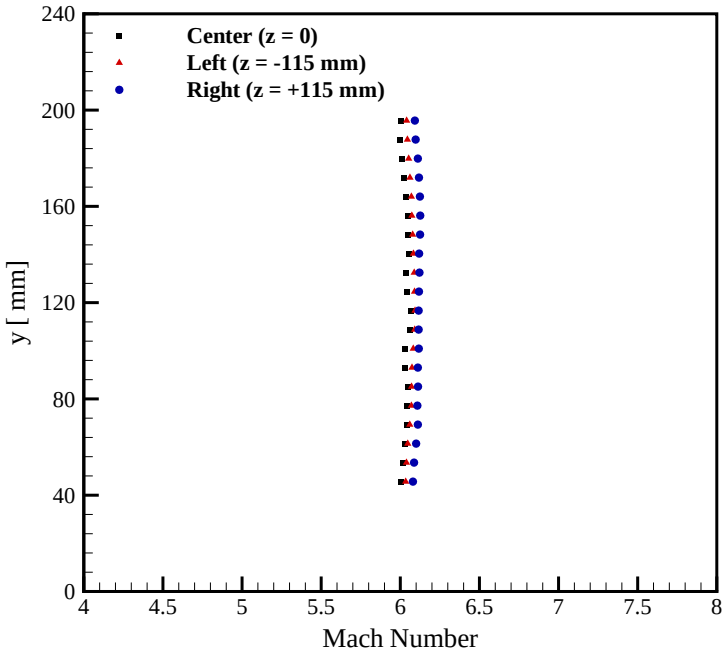

Figure 3.12: ACE Freestream Uniformity

Table 3.2: Flow Conditions

Mach No.	Re/m	P_t'/P_t [%]	P_0 [kPa]	T_0 [K]
5.65	$4.51x10^6$	1.4	448	425

thereby discouraging any instabilities and flow separation around the leading edge and underside ramp.

At the front of the plate, an interchangeable plug allowed for different trip geometries to be inserted. Shown in Figure 3.14 is the flat plate with the trip plug installed, and the four streamwise measurement locations selected for this experiment (dimensions in parentheses are scaled in terms of trip diagonal length as measured from the trip location).

The flow conditions for the current experiment are listed in Table 3.2.

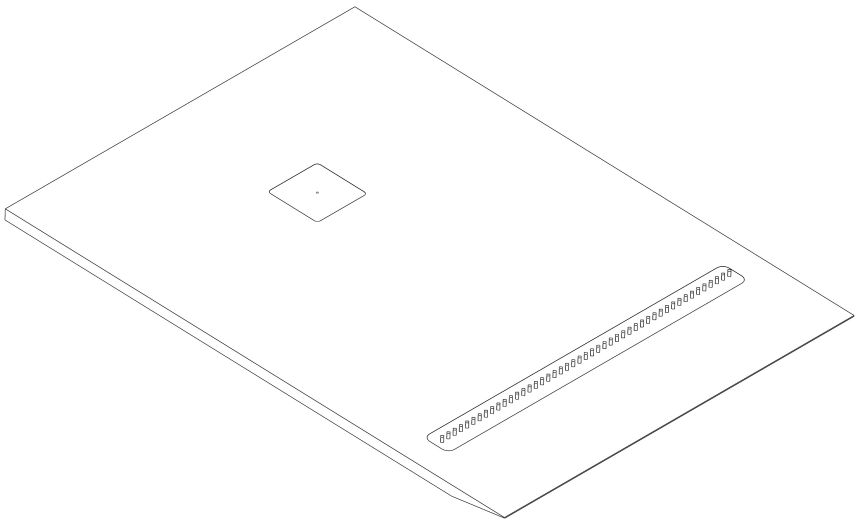

Figure 3.13: Flat Plate

3.2.2 Trip Selection

The trip geometry selected for the current experiment was modeled after the knowledge of the research conducted by Berry[7] et al. Colloquially, these trips are known as "pizza box," or "Trip 1" trips, and resemble individual diamond elements separated by some regular spacing. The trips with dimensions based on local boundary layer parameters are shown in Figure 3.15. The boundary layer height defined here is the point at which the total enthalpy recovers to 99.5% of the freestream value. Based on a laminar solution of the model at the test conditions, this boundary layer height was approximately $3.175mm$, which then defined the trip diagonal length to be $3.175mm$, with a center-to-center spacing of $6.35mm$. According to Berry et al., a trip height based on the current geometry of 133% the boundary layer height ($4.76mm$) is required to promote transition directly behind the trip.

For the baseline, smooth case, the front plug was a smooth surface which was machined while in the plate to eliminate any steps at the interfaces. When the

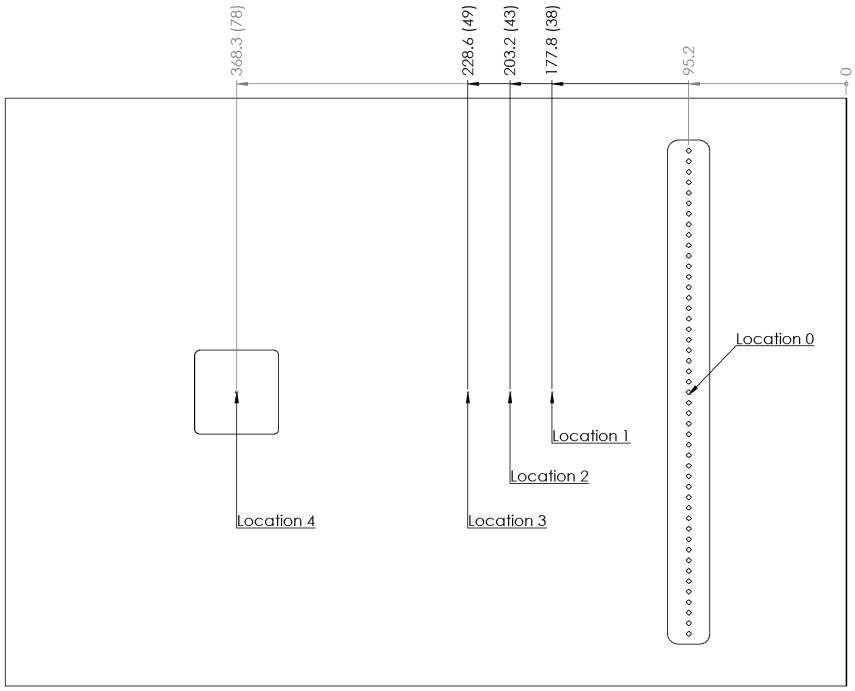

Figure 3.14: Measurement Locations

tripped plug was installed, shims were used to minimize interface steps down to less than $0.05mm$. Both plugs were sealed on the underside surface to prevent air leakage through the interface gaps.

3.3 Instrumentation

A variety of instrumentation techniques were used to acquire the data for this experiment. The techniques ranged from purely qualitative visual analysis, to multi-faceted quantitative measurements.

3.3.1 Schlieren

To visualize the flat plate boundary layer and flow structure generated by the trip elements, a single pass Z-type schlieren system was employed. A schematic of a typical schlieren system is shown in Figure 3.16. The mirrors used here were

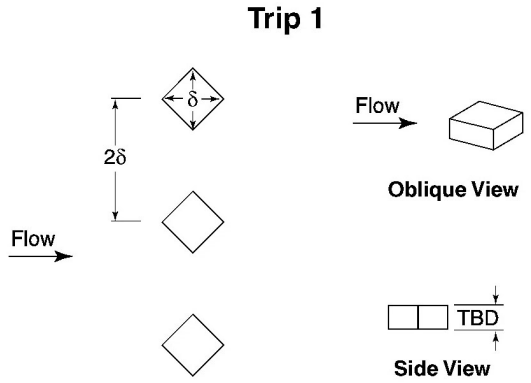

Figure 3.15: Trip 1 Geometry (Ref. 7)

152mm in diameter with a focal length of 914mm (f# of 6). An incandescent point light source with variable intensity (via a cutoff plate) was used to illuminate the field of view. On the imaging side of the system, a single razor blade was mounted on a multiple degree-of-freedom stage for maximum adjustability. The light passed through a 50mm focusing lens and then directly onto the CCD of a Nikon D5000 camera, which was controlled via Nikon's Camera Control Pro 2 software. Schlieren images were taken at both the primary measurement location (368.3mm, location 4), and at the trip location (127mm, location 0).

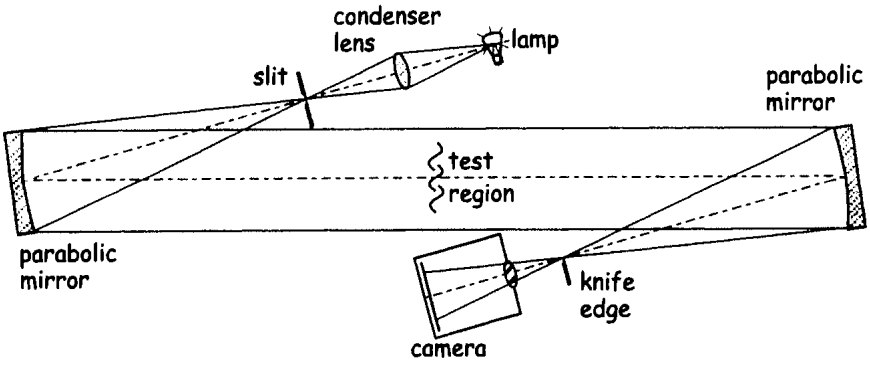

Figure 3.16: Schlieren Schematic (Ref. 64)

3.3.2 Surface Flow Oil Visualization

To visualize surface streamlines across the model, a mixture of silicone oil ($200cS$ viscosity) and "Blaze Orange" pigmented powder was painted across the entire model before a run (the model itself was painted black for added contrast). The model was installed in the tunnel, preheated to the appropriate temperature, and a full run was completed. After the run, the model was removed from the tunnel and photographed utilizing two high-intensity blacklights (courtesy of ISSI Corp.) to highlight the streamlines. Oil flows were taken for both the smooth plug and the trip plug cases. In addition, an oil flow was taken for a singular trip element using a mixture of silicone oil and titanium dioxide.

Due to the low-density nature of the facility and the necessity to preheat before a run to achieve the desired temperatures, a thick (thicker than normally used in supersonic/hypersonic facilities) coat of oil was required on the model. The large amount of oil is believed to have caused streamlines farther down the model to aggregate. This phenomenon is discussed in more detail in the results section.

3.3.3 Pitot Probe

At the final measurement location ($368.3mm$, location 4), extensive pitot probe surveys were conducted. The pitot probe was constructed from a $3.18mm$ diameter stainless tube (flattened on the exposed end for flow angularity sensitivity reduction), which was then soldered into a larger $6.35mm$ tube for support (the smaller tube was sealed from the larger tube, thus avoiding extra dead space to be evacuated from the volume). The tubing was connected to an Endevco 8540-15 pressure transducer (0-$103kPa$ full scale) outside of the tunnel, which was powered by an Endevco 136 amplifier.

A well-known fact regarding piezoresistive transducers is their tendency to drift (both zero offset and linearity) due to temperature changes. A temperature monitor circuit, as described in Reference 43, was built and added to the 8540-15 transducer to monitor its temperature during the run, and to allow for post-run corrections to the measured voltage. However, the experiment found that the temperature of the sensor chip on the transducer actually experienced a decrease from idle conditions to running conditions of nearly $10K$. As the transducer was mounted outside of the tunnel, it was hypothesized that the total temperature inside the test section ($425K$) did not have an impact on the transducer, and that rather, the evacuation of air during tunnel start-up led to the decreased temperature. This modest decrease in temperature did not have an appreciable effect on the voltage output, and therefore, no corrections were necessary.

Due to the low pressures encountered near the wall of the model ($< 2000Pa$), it was necessary to ensure the pitot probe "settled" for an appropriate amount of time at each height location to allow for pressure stabilization. In the outer edges of the boundary layer, a time of 0.5 seconds was found to be sufficient. However, at lower points in the boundary layer, this time was increased to 2 seconds to allow adequate equalization. The combination of movement time and settling time restricted the number of points that could be acquired in a single run, hence, multiple runs were conducted to acquire a sufficient number of data points. The real-time pressure was monitored through the auxiliary data acquisition system, and provided verification that the pressure had stabilized. Only average data were used for these measurements - fast response data is not available.

Pitot probe data were taken only at location 4, and across the span of interest as shown in Figure 3.17. Data for the laminar case (smooth plug installed) is not available, as the thinner nature of the boundary layer in addition to the shape of the

laminar boundary layer prevented the pitot probe from achieving stabilized pressure readings. Turbulent data (with the Trip 1 plug installed) were taken at location 4 and across the seven spanwise locations.

To determine the Mach number relative to the model, a static port was installed in the plate surface at location 4 and connected to an MKS Baratron 631C capacitance manometer ($13.3kPa$ range). The resulting total pressure as measured by the pitot probe divided by local static pressure was used to calculate local Mach number.

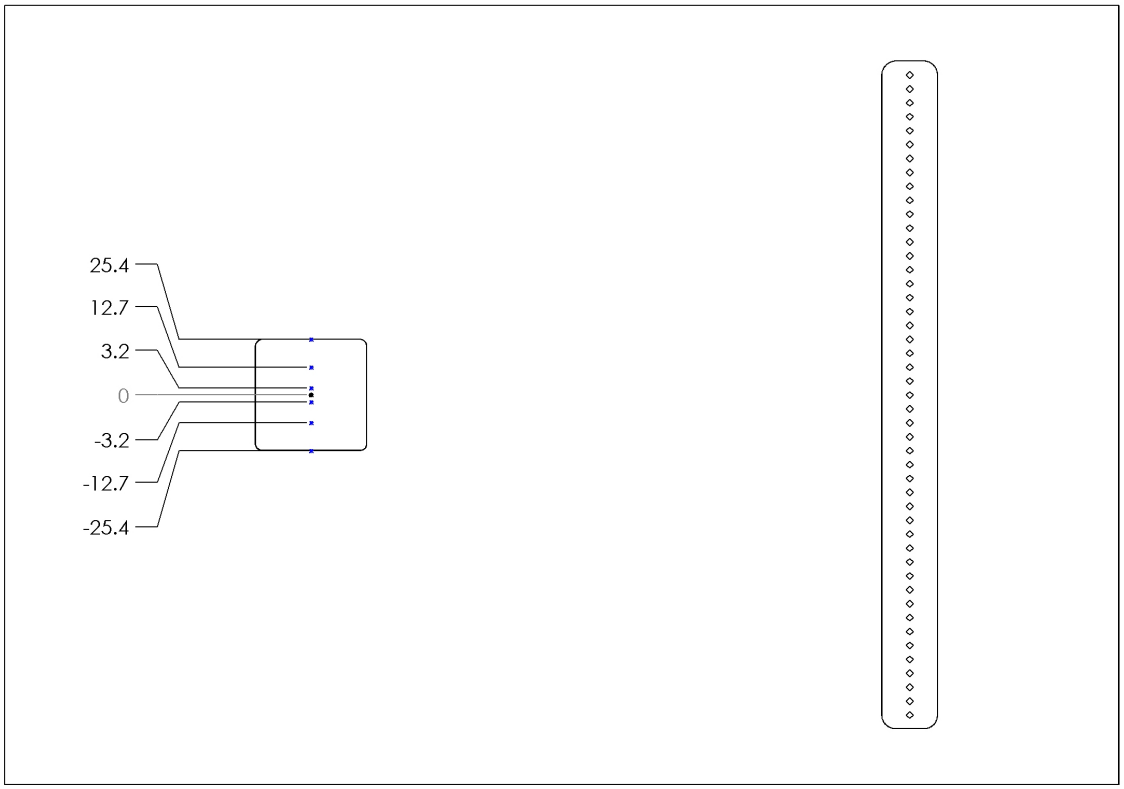

Figure 3.17: Spanwise Stations

3.3.4 Hot-wire Anemometry and Cold-wire Scans

Hot-wire data were also taken at location 4 across five of the spanwise stations, and at locations 1-3 along the model centerline. At each spanwise station of location 4, data were taken at three overheat ratios for the hot-wire runs, and one cold-wire run to measure mean total temperature. Data at locations 1-3 were only taken at the highest overheat ratio to provide an estimate of mass flux fluctuations and spectral content.

3.3.4.1 Hot-wire Probe

The hot-wires used for this campaign were manufactured by TSI and are model 1218HT-PI2.5 boundary layer probes (Figure 3.18). The probe consists of a single $2.5\mu m$ platinum-iridium (80%-20% combination) wire spot welded across two prongs $1.25mm$ in length. The entire length of the wire is exposed and active, giving an L/d ratio of 500. This high L/d ratio resulted in decreased frequency response. Data were sampled at $500kHz$ and a total of 100,000 samples were taken at each point in the boundary layer.

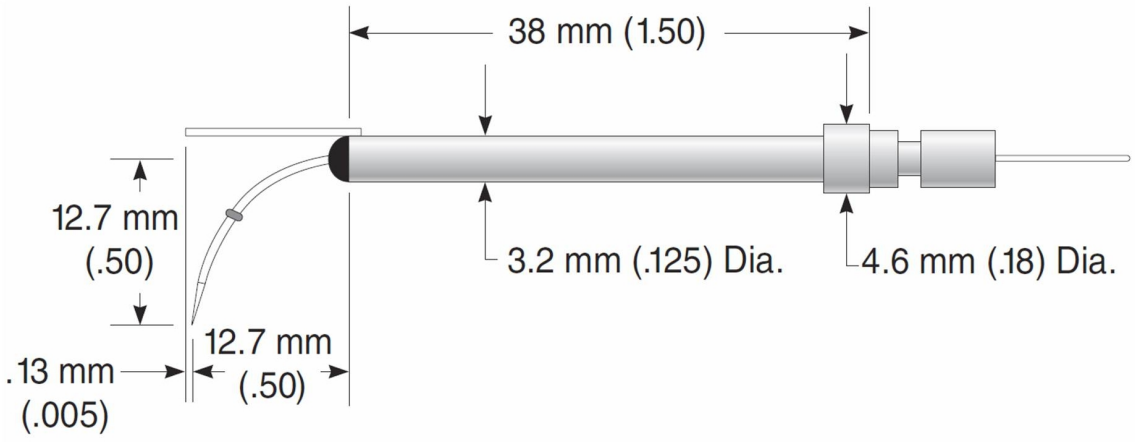

Figure 3.18: Boundary Layer Hot-wire Probe

Table 3.3: Hot-wire Parameters

Wire Resistance, Ω (Ohms)	Wire Temperature, T_{wire} (K)	Overheat Ratio, τ
15.2	780	0.8
14.7	650	0.5
14.0	590	0.2

3.3.4.2 Anemometer and Tuning Response

An A.A. Lab Systems AN-1003 multiple channel anemometer was selected to control the hot-wires. Using this anemometer, the wire resistance, bridge type (1:1 or 1:10), damping and amplification are all manually adjustable for optimum results. Table 3.3 lists wire resistances, temperatures, and overheat ratios used for this set of experiments. A total of three overheat ratios were used at each spanwise station of location 4. Using three independent overheats allows the hot-wire variables to be separated from one another (mass flux fluctuations, total temperature fluctuations, and the cross product of the two).

The hot-wire was tuned at the outer edge of the boundary layer (the area of highest fluctuations) using a simple pulse response test during an active run at test conditions. During initial tuning, the frequency response of the hot-wire was qualitatively judged by visualizing the response circuit on a digital oscilloscope. To quantitatively gauge the response of the anemometer circuit, a National Instruments PCI-5122 digitizer/oscilloscope card was connected to both the pulse output test signal from the anemometer, and the actual output of the anemometer. A digital FFT of the two signals allowed for real-time analysis of both the amplitude difference between the signals, and the phase lag. The point at which the signal dropped below the $-3dB$ point was determined to be the frequency response cutoff for the hot-wire. At the highest overheat ratio (0.8), the frequency cutoff was estimated to

be approximately $130kHz$. Note that the hot-wire was only tuned at the highest overheat, and spectral data is only available at this condition.

3.3.4.3 Cold-wire Measurements and Recovery Factor

In addition to running the hot-wire in operate (constant temperature) mode, the wire was also used in resistance mode (unpowered, not constant current) to perform a total temperature scan of the boundary layer. A Keithley 2000 Multimeter was connected to the hot-wire probe directly and controlled via the DAQ. At each point in the boundary layer, the hot-wire resistance was recorded. Using the measured resistance values from each run, the ambient temperature and ambient resistance of the hot-wire, and the calculated coefficient of resistance, the hot-wire temperature was computed. The hot-wire temperature, mass flux (converted to Reynolds number based on wire diameter) and the computed recovery factor (described below) were then used to calculate the total temperature of the flow.

By performing a mass flux (varying pressure, constant temperature) sweep at a known freestream Mach number and recording the wire resistances, it was possible to calculate wire recovery factor as a function of both wire Reynolds number, Re_d, and Knudsen number. The results from these measurements along with other data from Reference 32 are shown in Figure 3.19. The low densities, and corresponding high Knudsen numbers, are believed to be responsible for the high recovery factors seen in this facility.

3.3.4.4 Hot-wire Calibration

To obtain meaningful, numerical results from the hot-wire scans, it was necessary to calibrate the hot-wire at each overheat ratio. Estimates of the mass flux across the boundary layer led to the conclusion that the hot-wire could be calibrated across an appreciable range of mass flux values through a simple pressure sweep in a freestream

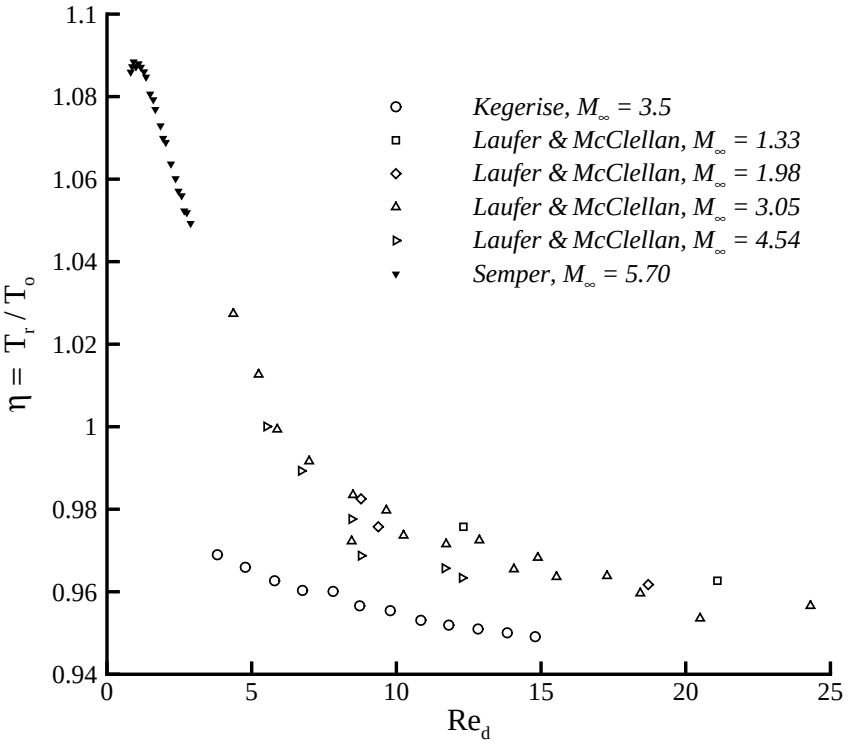

Figure 3.19: Hot-wire Recovery Factor vs. Wire Reynolds Number

region of known Mach number. Traditionally, the results from such a calibration are plotted as voltage squared versus mass flux, which is known as King's Law (Eqn. 3.1, Ref. 13),

$$V^2 = A + B(\rho u)^n. \tag{3.1}$$

However, the low density flow encountered in this facility led to a departure from the usual King's Law exponent of $n = 0.55$. The calibration data for each overheat ratio, along with curve fits, are shown in Figure 3.20. Noticeably, the calibration data more closely follow a linear fit than the traditional power law. Dewey's[20] technical report further verifies this result, and gives good confidence that low mass flux values

not obtainable in the calibration, but seen in the lower portions of the boundary layer, will still be accurate based on this linear calibration. For the hot-wire variable decomposition analysis, the calibration curves were computed from wire Reynolds number and Nusselt number (Figure 3.21).

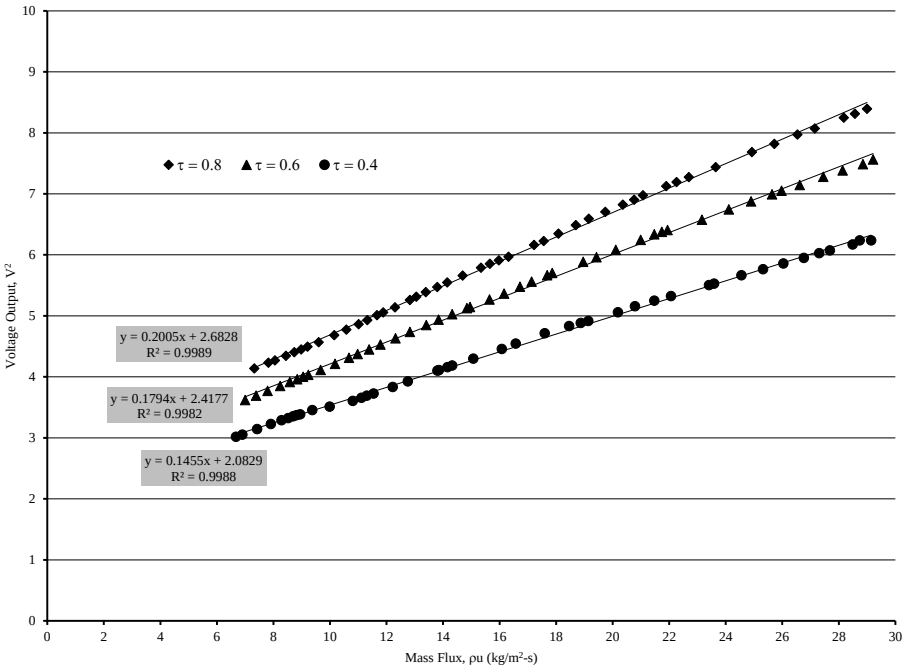

Figure 3.20: Hot-wire Calibration Curves, Mass Flux vs. Voltage

3.3.5 Traverse

To acquire multiple points across the boundary layer, an Aerotech ATS100-200 linear drive traverse with a BMS100 motor and Ensemble controller was selected (this combination added very little electrical noise to the system). The traverse was controlled via LabVIEW programs (thanks to Dr. Jerrod Hofferth for his expertise).

To determine probe flexing from idle configuration to active running, a simple visualization system was constructed. A Cooke pco.1600 camera was connected

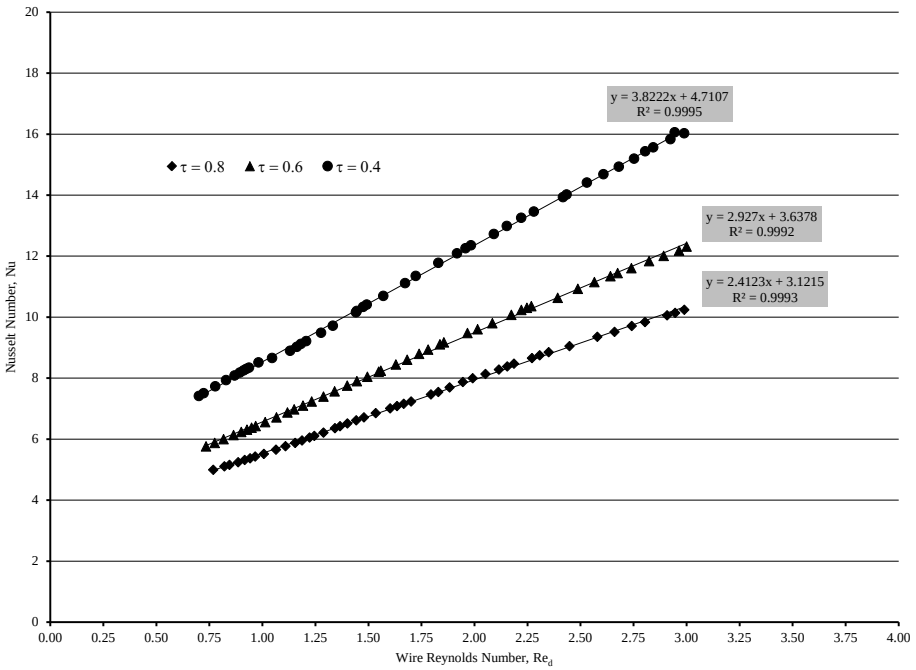

Figure 3.21: Hot-wire Calibration Curves, Reynolds Number vs. Nusselt Number

to a computer and focused on the probes (either hot-wire or pitot) using a Nikon $60mm$ lens. The camera was triggered with a signal from the DAQ whenever the program had reached a specific measurement point. Using this system, a collection of images was saved after each run corresponding to each measurement location in the boundary layer. Analysis of the images after the run (in addition to a "calibration image" utilizing a dot card) was useful to determine both the probe shift from start-up to steady state (less than $0.3mm$), and to ascertain if the traverse was moving correctly at each point without binding or stuttering.

3.3.6 Data Acquisition and Filtering

All pitot probe and hot-wire data were acquired on an NI PCI-6122 DAQ card that was capable of sampling 4 channels independently at $500kHz$. To prevent anti-aliasing from the hot-wire signal, the output from the anemometer amplifier was

passed through a Krohn-Hite FMB3002 filter with a fixed low-pass cutoff of $500kHz$ utilizing an 8-pole Butterworth circuit.

3.3.7 Post-processing Techniques

Data taken from the pitot probe surveys were considered steady state and were not used to analyze spectral content. The data points taken were averaged to give a total pressure which was then used to calculate the local Mach number. Converting the Mach number data to velocity data was accomplished using the Crocco-Busemann theorem, and is described in the results section.

The hot-wire data at location 4 were decomposed into their three independent variables following the procedure outlined in Appendix A, and discussed more in-depth in the hot-wire results section. Also shown in the results are the data from the single, high-overheat ratio conditions. Traditionally, a high-overheat ratio hot-wire is believed to be sensitive to only mass flux fluctuations, and not total temperature fluctuations. That theory is discussed by comparing the single overheat data to the multiple overheat data.

After total temperature was measured from the cold-wire scans, the resulting temperature profiles, and Mach profiles from the pitot data were used to calculate velocity. These results are then compared to the velocity as computed from the Crocco-Busemann theory.

Hot-wire data along the centerline at locations 1-4 were spectrally analyzed in MATLAB ('pwelch' command) using a 2500 point (200 Hamming windows with 50% overlap) FFT over the entire data record.

4. RESULTS AND DISCUSSION

The results from the current set of experiments are presented in this chapter, and are divided into the following sections, primarily separated by measurement technique,

1. schlieren results at the trip location as compared to CFD simulations, and schlieren results at the final measurements location to determine boundary layer thickness,
2. oil flow results along the entire plate for both untripped and tripped cases, and for a single roughness element as compared to CFD,
3. pitot probe results detailing Mach number profiles,
4. hot-wire mean profiles of mass flux and total temperature, hot-wire fluctuations of mass flux and total temperature, and hot-wire spectral content,
5. law of the wall plots from theory and combined pitot/hot-wire methods,
6. and the evolution of the boundary layer along the plate.

4.1 Schlieren

Using the technique described in Section 3.3.1, images were taken revealing the details of the boundary layer thickness and of the shock structure created by the trips at the leading edge of the model. At location 0 (the location of the trips), the schlieren photograph in Figure 4.1 clearly details the complex flow features created by this geometry. After the flow is compressed slightly by the 2° inclination at the leading edge of the plate, the incoming flow approaches the trips as the boundary

layer begins to grow. The trips are roughly 133% the boundary layer height, so the subsonic portion of the boundary layer "feels" the full presence of the trips well before the trips are actually encountered. This disturbance in turn leads to a region of slight flow recirculation and separation ahead of the trips, which in turn creates a compression that propagates downstream. Once the flow reaches the actual trips, the portions exposed to $M > 1$ generate oblique shock waves. Behind the trips, a wake region created by the counter-rotating vortex pair generated by the trailing edge of the trips causes the boundary layer to quickly increase in size. The vortex pair causes an upwash of lower velocity fluid from the lower portion of the boundary layer, while simultaneously creating a downwash of higher velocity fluid into the boundary layer.

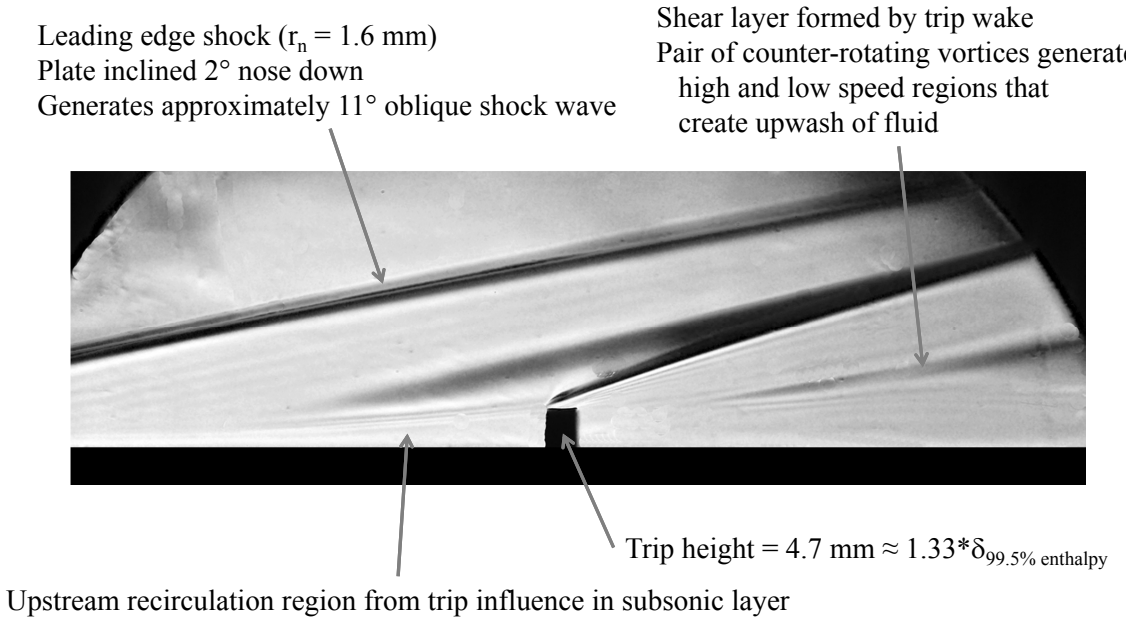

Figure 4.1: Schlieren Image of Trips (Location 0)

A laminar CFD solution was computed using the incoming flow conditions and the model geometry. The results of that simulation in comparison to the experimental results are shown in Figure 4.2, where the CFD contours represent Mach number. As indicated by the schlieren and CFD, the flow disturbances begin modifying the boundary layer thickness well ahead of the physical location of the trips.

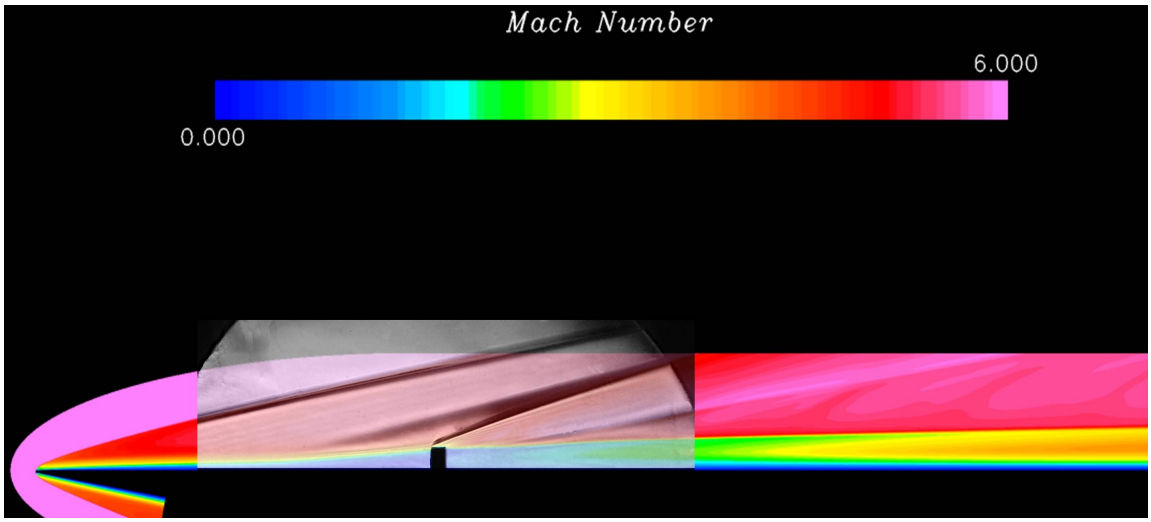

Figure 4.2: Schlieren Image of Trips - Comparison to CFD

At the final measurement location (location 4), schlieren images were also taken to determine the boundary layer thickness. Figure 4.3a represents the untripped boundary layer thickness, which is estimated to be approximately $8mm$. With the trips installed, the boundary layer grew to nearly $14mm$, as is shown in Figure 4.3b. These initial results provided confidence that the trips did indeed induce vortical disturbances into the boundary layer which eventually resulted in the breakdown of the laminar profile to turbulent. As a side note, an earlier experiment was conducted using a $10mm$ cylindrical rod at the leading edge of the plate. This "trip" had almost no effect on the boundary layer thickness, again reinforcing the idea that

3-dimensional trips are necessary to force transition in a hypersonic boundary layer.

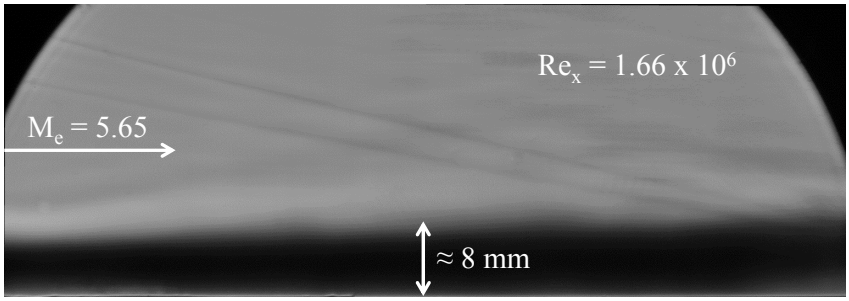

(a) Untripped Boundary Layer

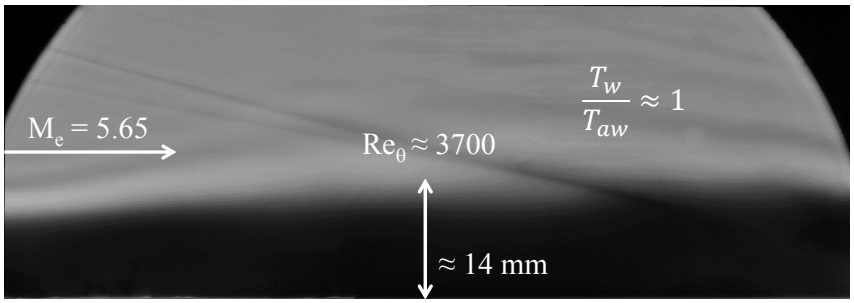

(b) Tripped Boundary Layer

Figure 4.3: Boundary Layer Thickness (Location 4)

4.2 Oil Flow

Results from the oil flow technique provided insight into the full-field flow over the model, as well as a more detailed insight into the flow around an individual trip element. The untripped flow field is shown in Figure 4.4. The primary purpose of the baseline case was to ensure there were no unexpected flow features (Mach lines, areas of separation) present on the model. However, there was a feature discovered here that was not anticipated. Since the current model spans the entire test section width, the nozzle side wall boundary layers (estimated to be $25 - 35mm$) impinge significantly onto the model. These boundary layers also continue to grow along

the model length. The growing boundary layers, or more importantly, the growing displacement thicknesses cause the model streamlines to converge towards the model center. Note the inconsistencies across the span of the model along the entire length.

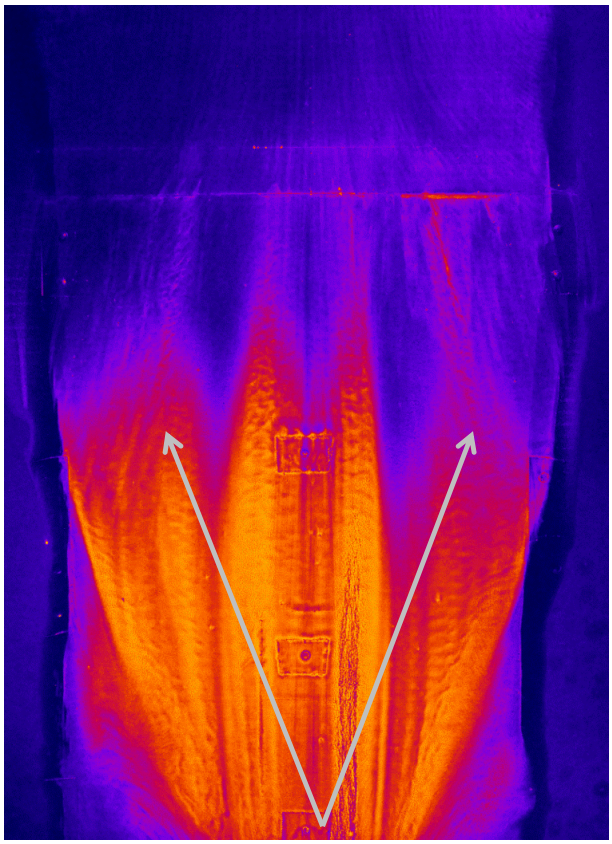

Figure 4.4: Oil Flow - No Trips

The converging effect is more noticeable in Figure 4.5 where the streamlines generated by the trip elements can be seen. At the front of the model, directly behind the plate, the streamlines flow parallel, but they quickly begin to converge as they traverse the model. In the tripped case, the flow is noticeably more uniform

across the span, indicating the trips had a "stabilizing" effect on any nonuniform aspects of the flow (very desirable from an engine inlet perspective).

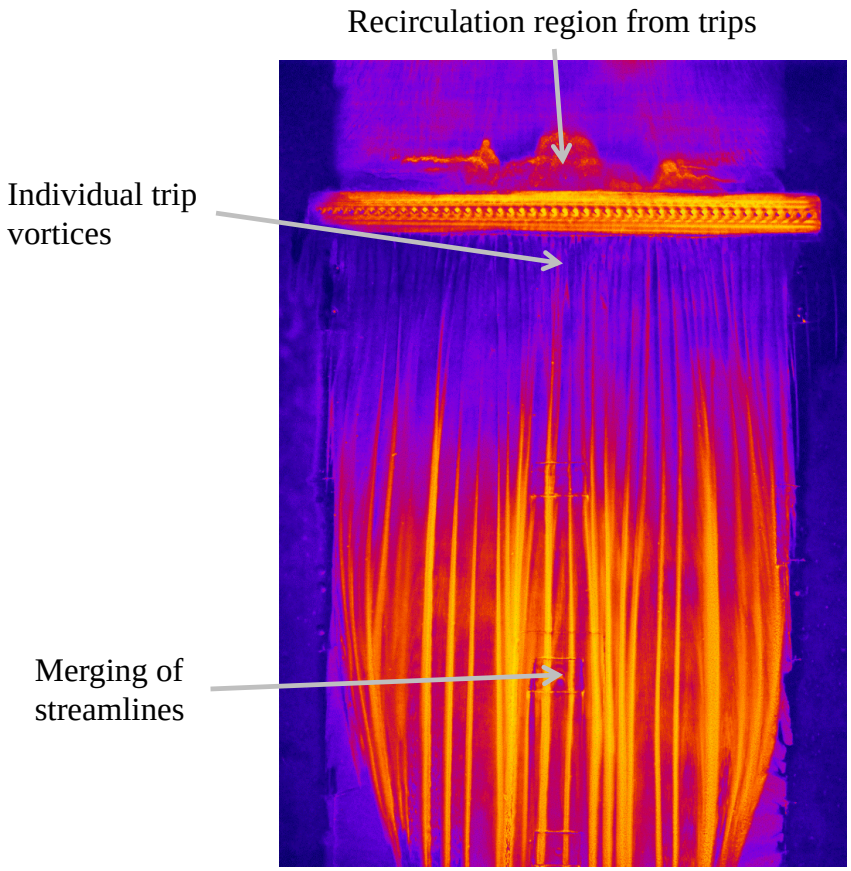

Figure 4.5: Oil Flow - Tripped

As was mentioned earlier, the low Reynolds number (low density) aspect of the ACE facility necessitated a thicker than usual coat of oil to properly visualize the surface streamlines. As a result of this thicker coating, it became impossible to determine if the streamlines downstream of the trips converged due to flow physics, or simply as a result from the aggregation of oil on the model surface. Ideally, the streamlines would follow the pattern shown in Figure 4.6 from Reference 7. In

that experiment, the individual streamlines generated by each trip element remain separated and distinguishable as they traverse the model. Regardless, the current oil flow did reveal the presence of the vortices generated by each trip element, and the stabilizing effect on the flow uniformity.

Choudhari et al. performed a time-accurate computational analysis of this trip geometry at Mach 3.5 and found results similar to the current experiment[16]. In their study, the streamwise velocity contours showed streaks that persisted for large distances behind the roughness element. The perturbation induced by the roughness element created a strong streamwise streak where fluid upwelling through the boundary layer increased the thickness substantially.

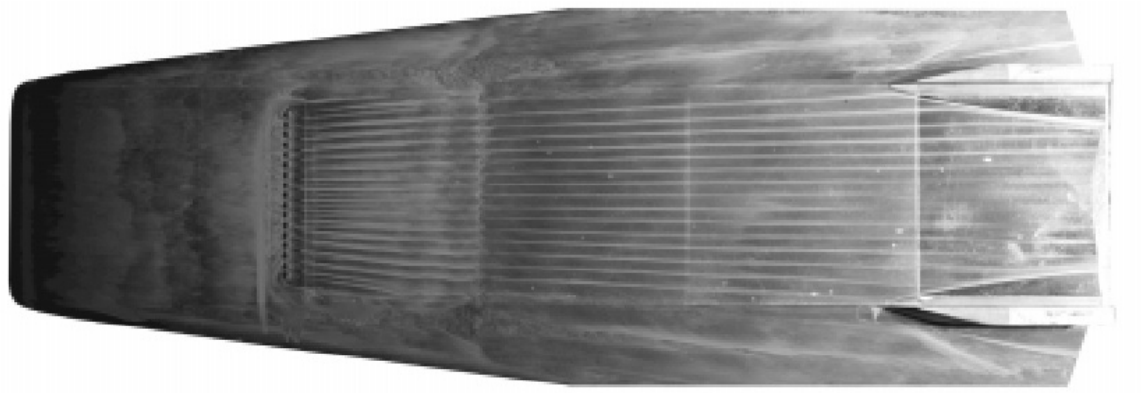

Figure 4.6: Oil Flow from Hyper-X Experiments (Ref. 7)

A single trip element was also examined using oil flow. In this case, the trip element was painted with a mix of silicone oil and titanium dioxide. After a full run, the flow field created by the trip element was captured in Figure 4.7. This oil flow reinforces the description in the previous section, and also verifies the CFD simulations that have been computed for this trip. Ahead of the trip, a large recirculation

region is created by the disturbances which propagate forward in the subsonic portion of the boundary layer. Then, a pair of counter-rotating vortices are generated from the sharp corners of the trip which create a shear layer that persists well into the boundary layer and well downstream of the trip location. A comparison of the CFD simulation with the oil flow over a single trip is shown in Figure 4.8. The color contours are of static pressure near the surface.

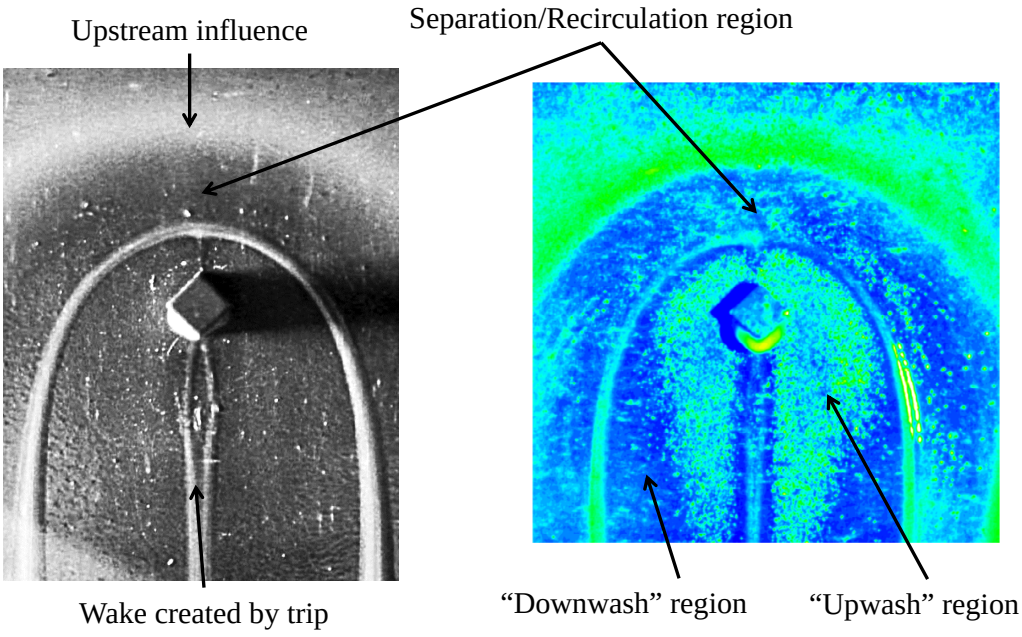

Figure 4.7: Oil Flow Around a Singular Element

4.3 Pitot Probe - Mach Number Profiles

Pitot pressure data were recorded at location 4 across the seven spanwise locations shown in Figure 3.17. The average total pressure at each boundary layer point was divided by the local static pressure (assumed to be constant throughout a run) to compute a local Mach number. The results for all of the measured stations are shown

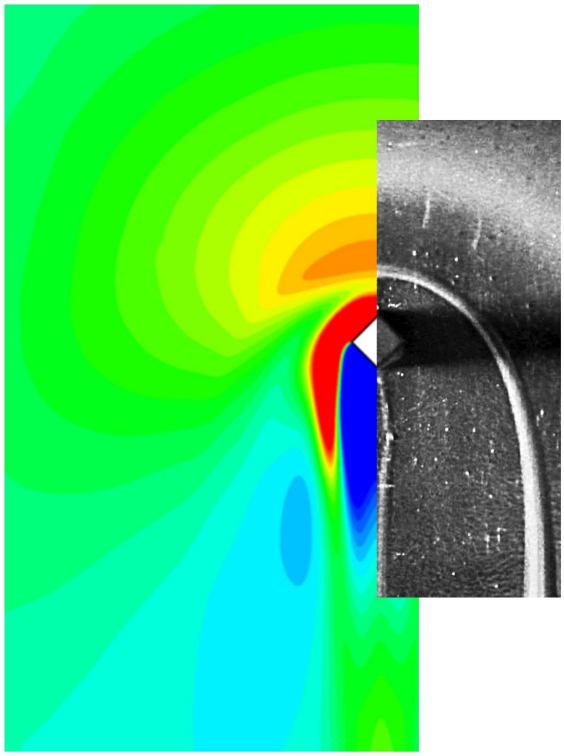

Figure 4.8: Trip 1 Oil Flow Compared to CFD

in Figure 4.9a. To better account for spanwise variation, the data were scaled by edge Mach number and boundary layer thickness in Figure 4.9b.

The measured profiles are in good agreement with one another, with only slight variations in the freestream Mach number and boundary layer thickness. On the negative spanwise side of the plate, there appears to be an indication of nonuniformity across the span. This slight defect in the Mach number profile could be caused by a location that is more transitional than turbulent, a strong presence of merging wakes, or simply a misalignment of the model resulting in a slight pressure gradient in the spanwise direction.

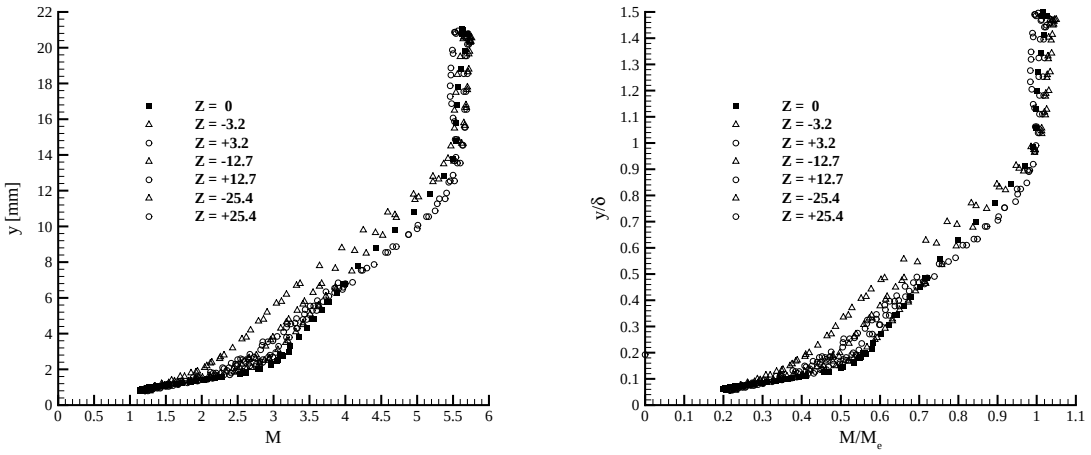

(a) Mach Number Profiles (b) Scaled Mach Number Profiles

Figure 4.9: Mach Number Profiles (Location 4)

To better visualize the uniformity of the flow across the plate, the Mach number profiles were combined to create a contour plot, shown in Figure 4.10. As illustrated by the contours, the flow is mostly uniform, with slight differences (thicker boundary layer) on the negative locations. Up to the $1.5mm$ height location, the contours appear uniform across the boundary layer, indicative of the subsonic and low supersonic portions of the flow being relatively unaffected by trip wakes or pressure gradients. As will be discussed in the recommendations, a spanwise traverse at several boundary layer heights can better address these questions.

4.4 Hot-wire

The data acquired from the hot-wire and cold-wire scans at location 4 across five of the spanwise stations are presented here. The data is divided into single overheat ratio data, cold-wire data, multiple overheat ratio data, and spectral content.

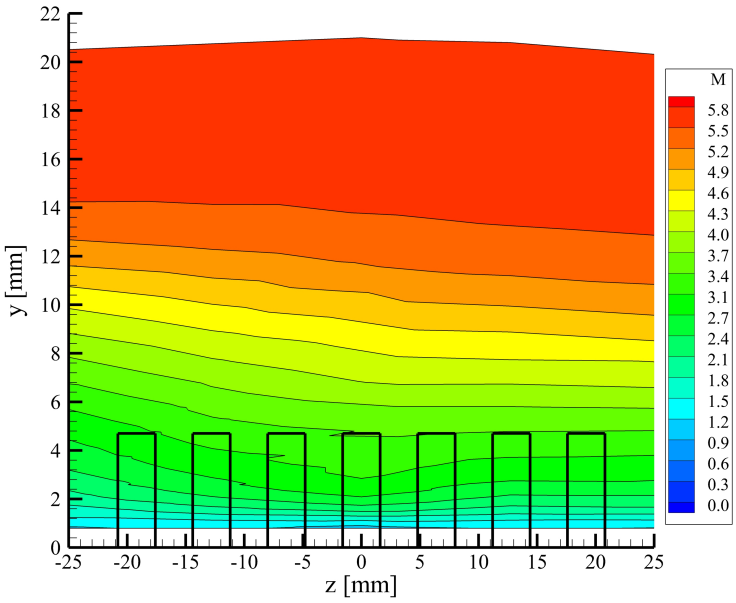

Figure 4.10: Mach Number Profiles Across Span (Location 4)

4.4.1 Single OHR Data

Using a single, high overheat ratio (OHR, $\tau = 0.8$), it was possible to estimate the mass flux and mass flux fluctuations in the flow. While anemometers are sensitive to mass flux and total temperature fluctuations, it is generally believed that operating at high OHRs decrease the sensitivity to total temperature fluctuations to negligible levels. In Figure 4.11a, the mean mass flux profiles across the spanwise stations are compared. Also shown for reference is the untripped profile. The data show good agreement, with only a slight departure at one of the stations. The untripped profile is noticeably different from the tripped profiles, and is indicative of laminar flow (thinner boundary layer and shallower profile).

The mass flux fluctuation levels, shown in Figure 4.11b are also relatively similar. Typical of turbulent boundary layers, the peak RMS value of the mass flux fluctuations is a "dull" peak, spread across a large region of the boundary layer.

The evolution of this peak is discussed further in Section 4.6. The fluctuation levels decrease in the lower boundary layer as wall effects and viscous damping become more prominent..

Again, as with the Mach number profiles, the data are scaled by the boundary layer edge mass flux values and boundary layer thickness to produce Figure 4.12a. With this scaling, the mean profiles and fluctuating profiles are all identical. The peak value of fluctuations occurs at roughly 80% of the boundary layer height and is equal to about 3% of the freestream mass flux. As an additional comparison, the fluctuation levels can also be scaled by the local mass flux values. Shown in Figure 4.12b, when scaled in this manner, the fluctuation levels appear to increase closer to the wall as the fluctuation level becomes a larger percentage of the local mass flux.

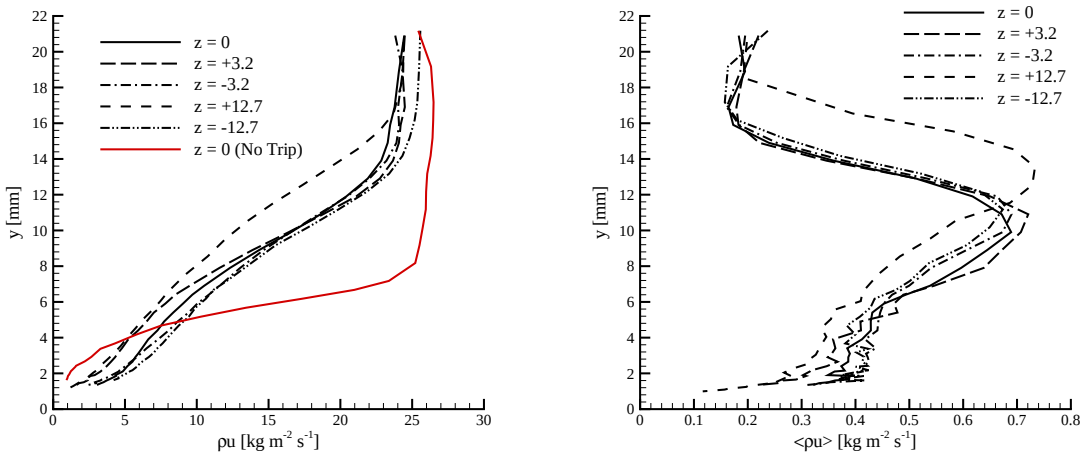

(a) Mean Mass Flux (b) Mass Flux Fluctuations

Figure 4.11: Single OHR Mass Flux & Fluctuations (Location (4)

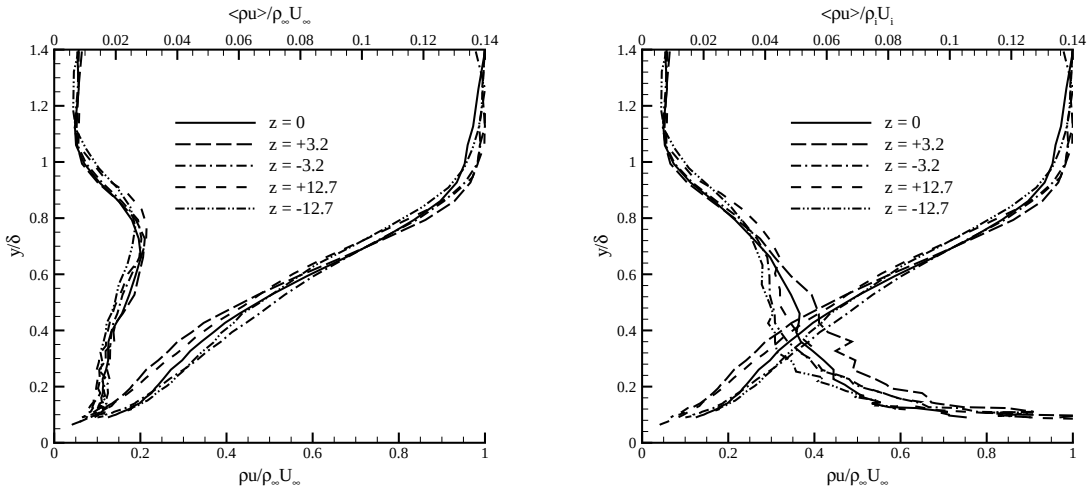

(a) Scaled Mass Flux (By freestream) (b) Scaled Mass Flux (By local values)

Figure 4.12: Single OHR Mass Flux & Fluctuations, Scaled (Location 4)

4.4.2 Cold-wire Data

Total temperature profiles, measured by using the cold-wire technique described in Reference 32 were also acquired at location 4 across the five spanwise stations. The comparison of unscaled total temperature profiles is illustrated in Figure 4.13a, and the scaled profiles are shown in Figure 4.13b. A primary reason for the scatter exhibited in both figures is the inability of the current facility to remain at a constant total temperature throughout a run, and the difficulty in repeating exact temperature conditions from run to run. Nevertheless, the data are similar, and the profiles are representative of typical hypersonic boundary layer temperature data. The temperature profiles were used to calculate velocity throughout the boundary layer based on the Mach number data.

4.4.3 Multiple OHR Data

Following the methods in Reference 11, and solving the equations derived in Appendix A, the multiple overheat data were reduced. By using all 3 overheat ratio

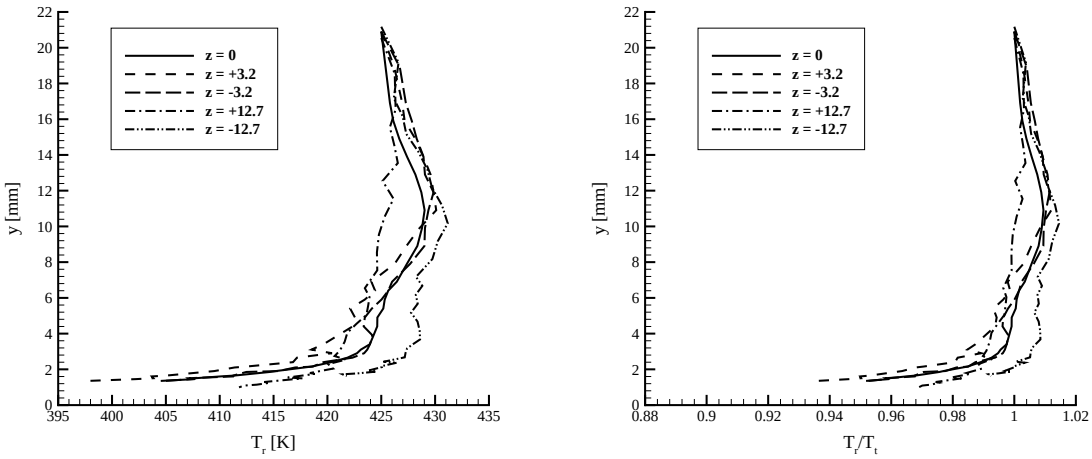

(a) Mean Total Temperature (b) Scaled Mean Total Temperature

Figure 4.13: Total Temperature Profiles, Cold-wire (Location 4)

hot-wire scans, the fluctuating quantities $\overline{(\rho u)'^2}$, $\overline{(\rho u)'T_0'}$, and $\overline{T_0'^2}$ were computed. In Figure 4.14a, the mass flux fluctuations from this method are presented and compared to a single location measurement using the single OHR method. The results appear to be different (with single OHR underpredicting) by about 2%, which is the approximate level of temperature fluctuations shown in Figure 4.14d. This result does reinforce the idea of using high OHRs to determine mass flux fluctuations only, but also demonstrates the still slight sensitivity to temperature fluctuations.

When examining the data from the multiple OHR cases, it becomes apparent that the data exhibit far more scatter than in the single OHR case, and the cross product and total temperature fluctuations appear to exhibit no uniformity in the spanwise direction. However, due to the nature of the experiment, it is not clear if these results are accurate. The three OHR scans were performed on three separate runs, during which conditions were not identical. As will be mentioned in the recommendations section, a better approach would be to use a hot-wire scanning circuit to cycle through a number of OHRs at each point in the boundary layer during a single run.

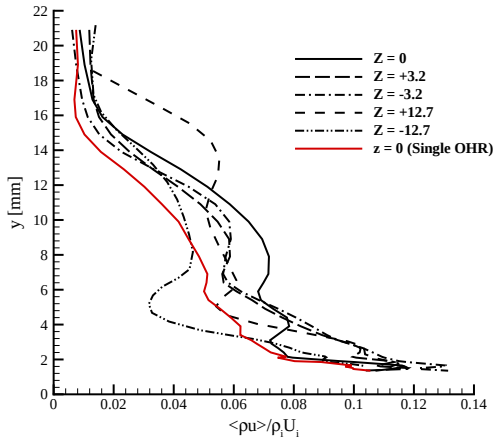

(a) Mass Flux Fluctuations

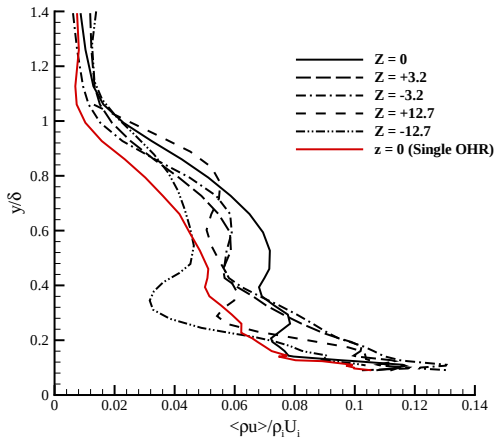

(b) Scaled Mass Flux Fluctuations

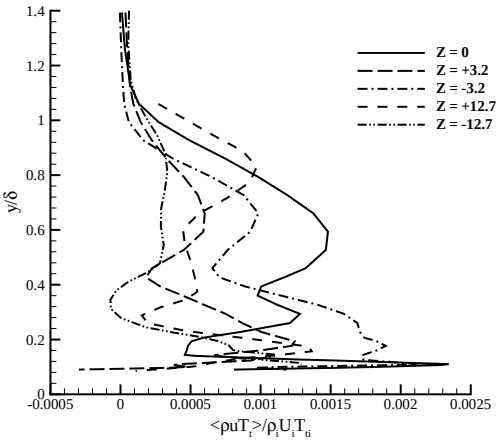

(c) Cross Product Fluctuations

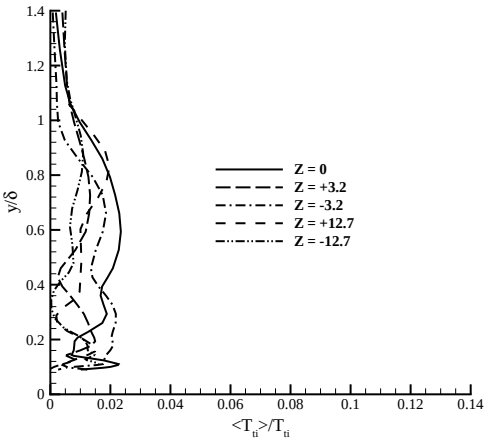

(d) Total Temperature Fluctuations

Figure 4.14: Multiple OHR Data (Location 4)

4.4.4 Spectral Content

At the highest OHR of each spanwise measurement location, spectral data is available up to the Nyquist acquisition frequency of $250kHz$. A contour plot showing spectral energy density across the boundary layer is shown in Figure 4.15. For the untripped case, represented in Figure 4.15a, the region of high energy content is significantly smaller than the tripped case shown in Figure 4.15b. The frequency bandwidth of the tripped condition (at the peak location of fluctuations) also appears

to be twice as large (from $50kHz$ to $100kHz$) as the untripped condition. This increase in energy scales can be attributed to the large scales generated by the trips. With more large scales with higher initial energy content, the breakdown to smaller scales can persist longer before viscous dissipation becomes important, creating a larger number of small scales (the smaller the scale, the higher the frequency).

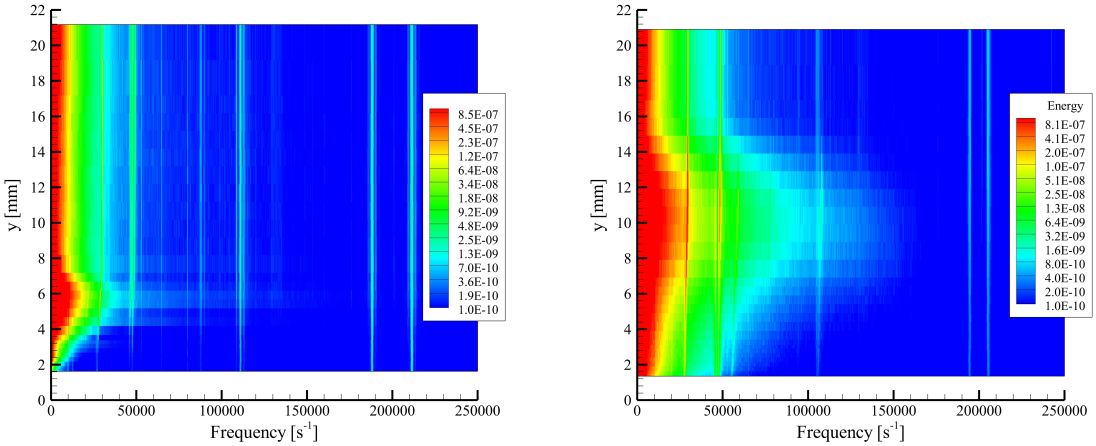

(a) Untripped Boundary Layer (b) Tripped Boundary Layer

Figure 4.15: Untripped & Tripped Power Spectra (Location 4)

A selected number of points from each boundary layer condition was extracted and the results are shown in Figure 4.16. The black lines in each, corresponding to freestream conditions, are very similar. For the untripped case, there is a slight increase in overall amplitude near the 67% thickness region in the boundary layer, followed by a large decrease (approaching electronic noise levels of the anemometer). The fluctuations appear to damp out quickly, and one would expect to see second mode content at high enough (and in quiet conditions) frequencies.

In the tripped case, the peak disturbance region in the boundary layer sees a similar increase to that of the untripped case, but as was mentioned previously, the

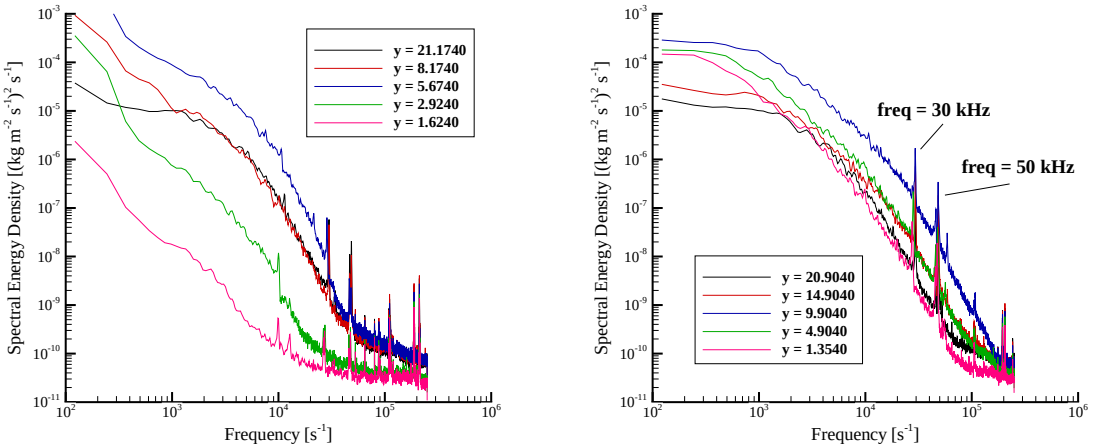

(a) Untripped Boundary Layer

(b) Tripped Boundary Layer

Figure 4.16: Untripped & Tripped Power Spectra at Selected Heights (Location 4)

frequency range is nearly double. The amplitudes then decrease as well, but they do not drop as rapidly as the untripped condition. The curves would be expected to continue to decrease as the wall was approached, but this effect is difficult to measure due to the steep nature of the turbulent boundary layer velocity profile.

Present in both cases are spectral peaks near $30kHz$ and $50kHz$. When scaled by freestream velocity ($850m/s$), the resulting length scales are $28mm$ and $17mm$ respectively. The presence of these peaks in both cases suggests that they are artifacts generated by the tunnel environment. Indeed, at these calculated length scales, the peaks could be generated by radiant noise from the nozzle or side wall turbulent boundary layers.

As first hypothesized by Kolmogorov[36], the turbulent power spectra should scale according to energy dissipation and flow length scales. According to dimensional analysis, the length scales should be raised to the $-5/3$ power. The power spectra for two selected points in the turbulent, tripped boundary layer are presented in Figure 4.17a. The first plot is scaled in terms of frequency, and the second by wavenumber.

When shown with a power law curve fit at the appropriate slope, the spectra do appear to follow the expected trend. The larger scales ($1kHz$) down to the smaller scales ($10kHz$) follow the curve fit, with the spectra rolling off at a higher rate after that point.

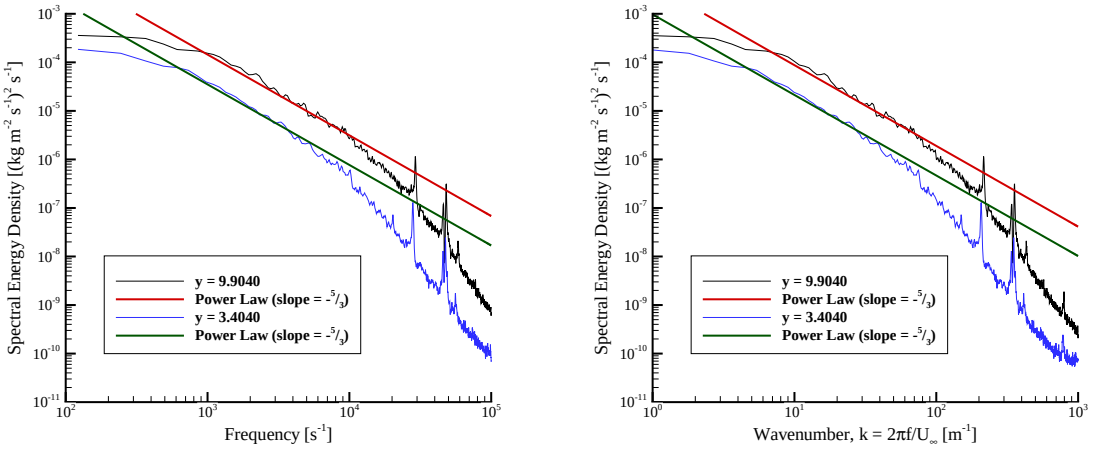

(a) Power Law Fit (Frequency) (b) Power Law Fit (Wavenumber)

Figure 4.17: Turbulence Power Spectra Scaling, Mass Flux Fluctuations

4.5 Law of the Wall

One of the fundamental theories of turbulence is the ability to scale local flow properties by boundary conditions to create a self-similar plot known as the "Law of the Wall." The inner scaled variables are defined in Equation 4.1 (note that the subscript denoting wall conditions implicitly defines these relations for the compressible flow case). For the current experiment, wall temperature and wall pressure are known, so wall density can be calculated from the simple equation of state. Wall shear stress is typically difficult to measure, and in most cases it is estimated by fitting the data to the law of the wall equation (by fitting the innermost data points

to the laminar sublayer data). In the current experiment, a Preston tube was used to attempt to measure wall shear stress. While the tube used was not circular (it was flattened, as most pitot probes are), the results at least provided a rough estimate. Following the work of References Hopkins[28] and Keener[30], the wall shear stress was calculated to be approximately $12Pa$, (resulting in a friction velocity of approximately $61m/s$).

$$\begin{aligned} u^+ &= \frac{\bar{u}}{v^*} \\ y^+ &= \frac{yv^*}{\nu_w} \\ v^* &= \left(\frac{\tau_w}{\rho_w}\right)^{1/2} \end{aligned} \tag{4.1}$$

To properly scale the flow variables, the streamwise velocity is needed. In the current experiment, however, the velocity was not measured directly, only Mach number. For flows with constant specific heat and negligible pressure gradients, the Crocco-Busemann relation between velocity and temperature can be used (Equation 4.2). By assuming adiabatic wall conditions (a valid assumption for the current experiment), a similar equation can be derived in terms of Mach number and ratio of specific heats (Equation 4.3). Having now calculated the local (static) temperature across the boundary layer, the local speed of sound can be calculated, and from speed of sound and Mach number, local velocity.

$$\bar{T} \approx T_w + (T_{aw} - T_w)\frac{\bar{u}}{U_e} - \frac{r\bar{u}^2}{2c_p} \tag{4.2}$$

$$\bar{T} = \frac{2T_w}{rM^2(\gamma - 1) + 2} \tag{4.3}$$

Van Driest used the Crocco-Busemann relation in addition to a mixing length theory that accounted for variable density to define a new "effective velocity" to scale compressible experiments to the incompressible law of the wall data (Equation 4.4).

$$u_{eq} = \frac{U_e}{a} \sin^{-1}\left(\frac{a\bar{u}}{U_e}\right) \tag{4.4}$$

Using the above equations and the pitot probe data, it was possible to recreate the law of the wall plots. Figure 4.18 present the data with the typical law of the wall regions: the laminar sublayer, overlap region, and log region with "accepted" constants of 0.4 and 5.5. To properly set the location of the data points, the wall shear stress was selected to be $11.6Pa$, which is only a 3% difference from the Preston tube data. Again, all of the data are very similar (Figure 4.18d), with the one outlying set of data at the $-25.4mm$ station. Along the centerline (Figure 4.18a), the data overlap well, and even follow the log region of the law of the wall using accepted values. The final values (closest to the wall) even indicate good agreement with the linear theory used in the laminar sublayer (and suggest the pitot measurements were able to reach this region). However, noticeably missing from these data is the existence of the overlap region between laminar sublayer and log layer. Such a departure from theory could be an effect of the low Reynolds numbers encountered here.

While the assumptions used in the Crocco-Busemann derivation seem valid for the current experiment, a comparison between those velocity values and actual velocity values was made. Using the temperature profile measurements from the cold-wire scans and the Mach number profiles, it was possible to compute local static temperature based on the isentropic relations. This new temperature was then used to

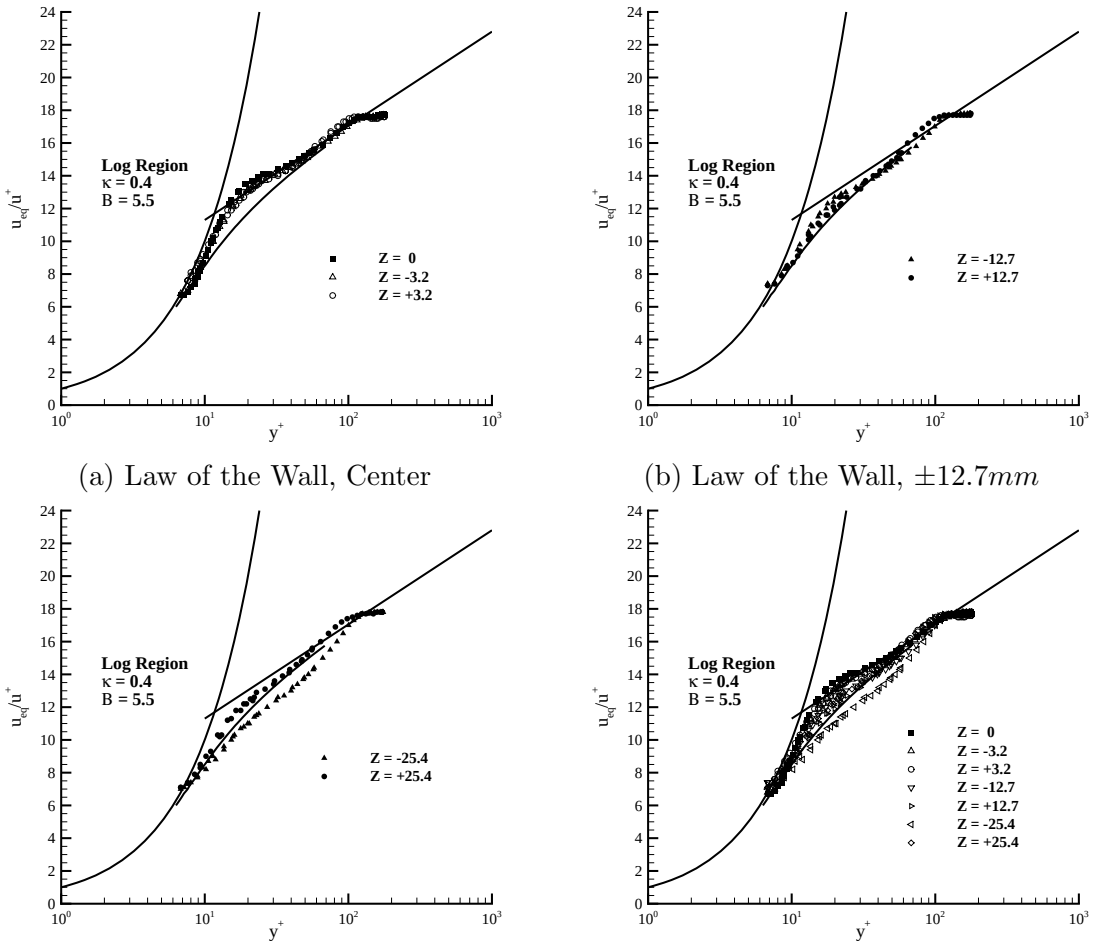

(a) Law of the Wall, Center

(b) Law of the Wall, $\pm 12.7mm$

(c) Law of the Wall, $\pm 25.4mm$

(d) Law of the Wall, All Locations

Figure 4.18: Law of the Wall (from Crocco-Busemann)

calculate local velocity, and the law of the wall plot was recreated. The comparison between Crocco-Busemann and "measured" velocity is shown in Figure 4.19 for the centerline location. Both sets of data agree very well, and can even be made to match identically with small changes to the recovery factor. While this experiment is assumed to be at adiabatic wall temperature, it is in fact 1-2% cooler, which can account for this slight difference.

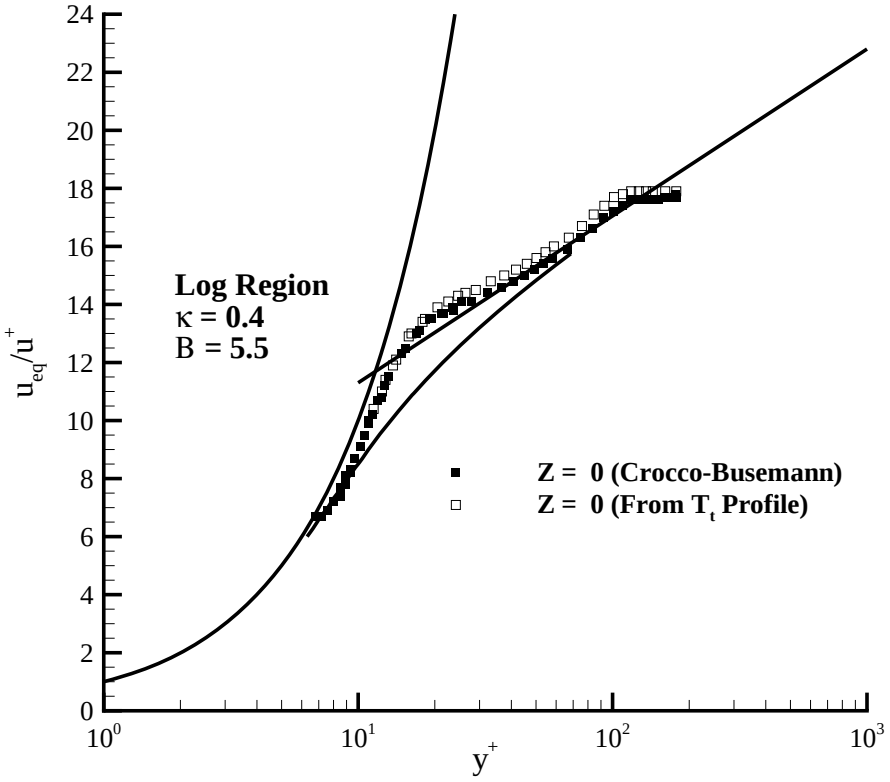

Figure 4.19: Law of the Wall, Comparison at z = 0

4.6 Streamwise Profiles

Measurements taken along streamwise stations 1-4 with the hot-wire operated at the highest OHR are shown in Figure 4.20. The mean mass flux is plotted in Figure 4.20a, and an interesting phenomenon is discovered. The trips selected specifically for this experiment were expected to cause transition directly downstream of the trailing edge. However, as Figure 4.20a would suggest, the boundary layers remain laminar at locations 1-3 (as evidenced by the similarity to the untripped profile at location 4). When scaled by boundary layer height in Figure 4.20c, the traditional profiles of laminar (shallow) and turbulent (full) are revealed. The distance from location 3 to location 4 is approximately $130mm$, and transition to full turbulence

must occur in this region.

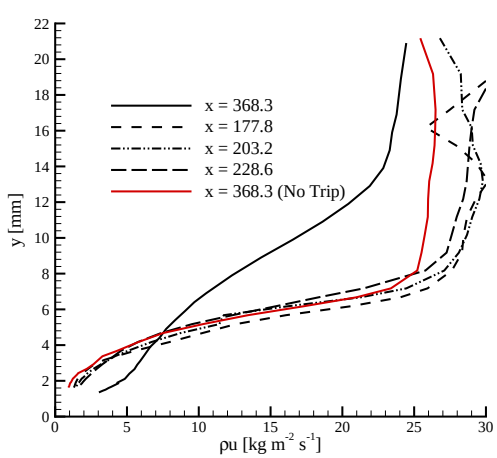

(a) Mean Mass Flux, Streamwise

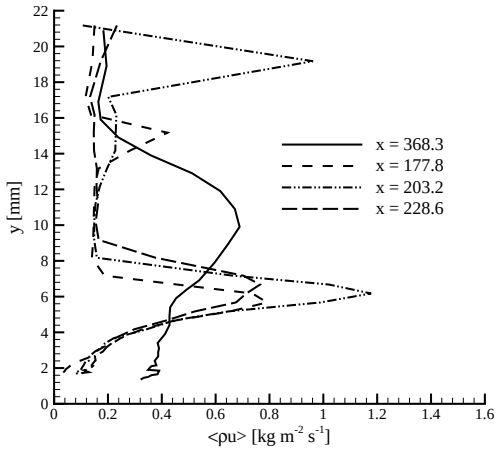

(b) Mass Flux Fluctuations, Streamwise

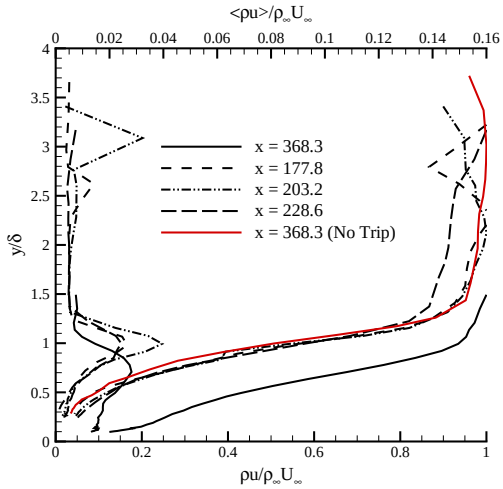

(c) Scaled Mass Flux Values, Streamwise

Figure 4.20: Streamwise Hot-wire Data (Locations 1-4)

Assuming the hot-wire is primarily sensitive to mass flux fluctuations at this high OHR, the mass flux fluctuations were calculated and are plotted in Figure 4.20b. Even though this experiment was conducted in a conventional tunnel and not a "quiet" facility, the trend observed in Reference 32 is still apparent. As the

hot-wire is moved downstream of the roughness element, the peak RMS value of the mass flux fluctuations increases in magnitude until some critical value is reached. After that value, the peak decreases slightly, but the width of this peak increases, indicating a broadening of the disturbance levels throughout the entire boundary layer. The large peaks towards the upper end of the measurement range are believed to be from the leading edge shockwave generated by the plate.

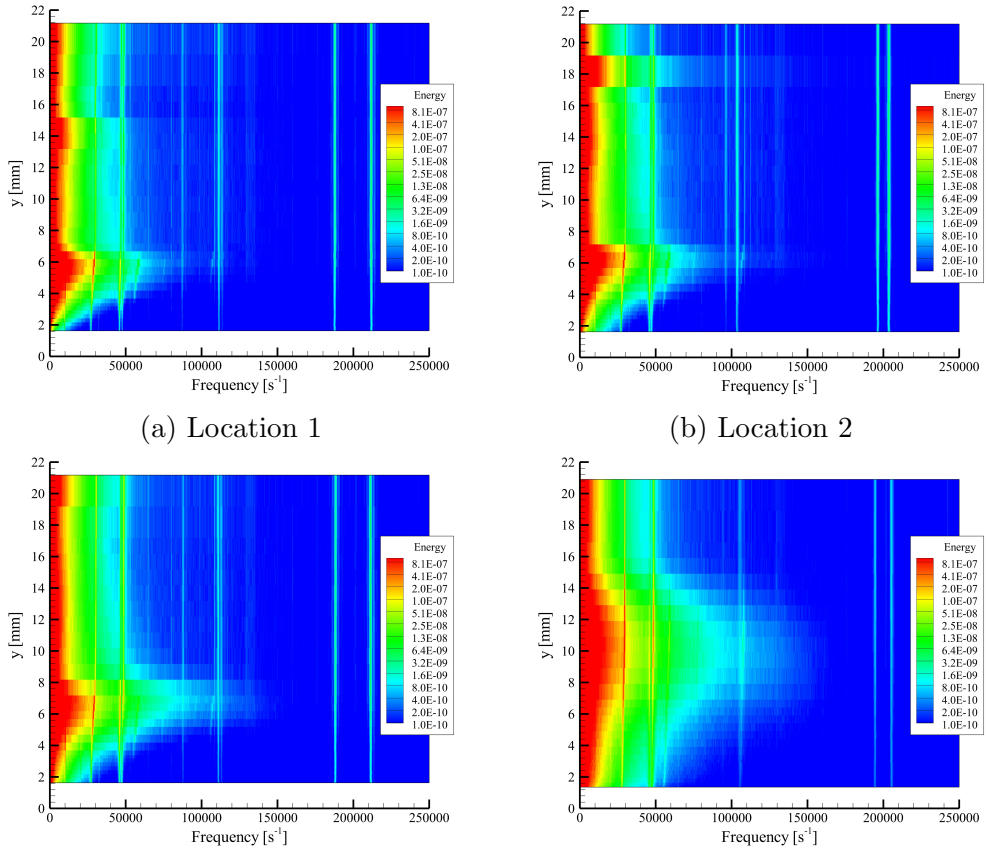

(a) Location 1

(b) Location 2

(c) Location 3

(d) Location 4

Figure 4.21: Power Spectra Along Streamwise Locations

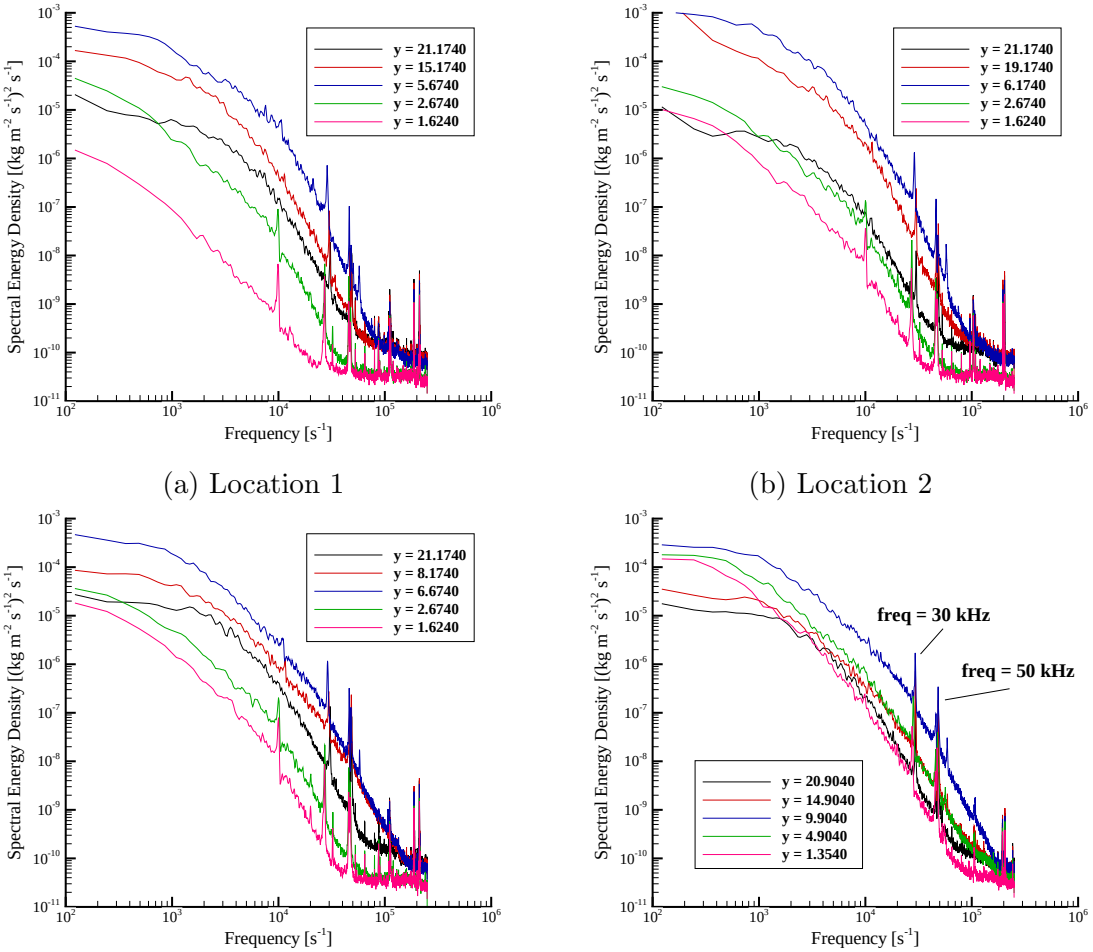

(a) Location 1

(b) Location 2

(c) Location 3

(d) Location 4

Figure 4.22: Power Spectra Along Streamwise Locations (Selected Heights)

An examination of the spectra from each location reveals a similar trend (Figures 4.21 and 4.22). The location of the max RMS (blue lines in the line plots) remains at the same intensity, but its location in the physical boundary layer is rising. Also note that the fluctuation intensity from location 1 to 2 near the wall increases by an order of magnitude, but does not change significantly from location 2 to 3.

Following the work of Kegerise[32] et al., the spectral content at each streamwise location is plotted at the boundary layer height location where the RMS fluctuation

level reaches its peak. The spectra of each location at these points in the boundary are similar (Figure 4.23a), with the spectra of the untripped boundary layer being lower in amplitude above $10kHz$ and experiencing a more pronounced roll-off. Unfortunately, the broadband noise and the background noise make it impossible to distinguish second mode waves or breakdown. However, when zoomed in, a peak at $58kHz$ is clearly visible in the tripped cases that is not present in the untripped case. The presence of this peak in the tripped cases is believed to be caused from the vortex shedding from the trips. The Strouhal number is a fluid mechanics parameter that relates vortex shedding frequency, characteristic length, and velocity. Using the measured frequency, the trip characteristic length (diagonal of $3.2mm$), and the freestream velocity ($850m/s$), the Strouhal number is 0.217, very near the classical value of 0.2.

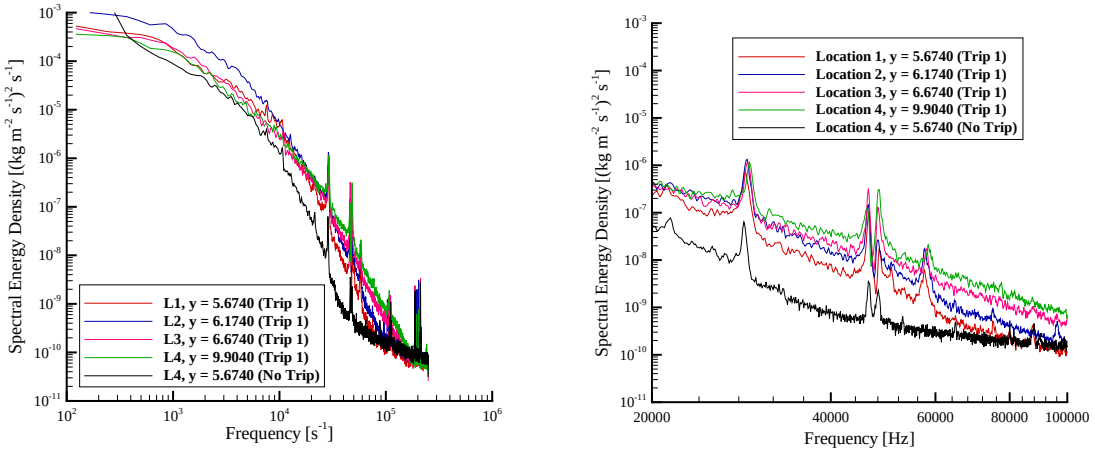

(a) Power Spectra at Max RMS

(b) Power Spectra at Max RMS (Zoom)

Figure 4.23: Power Spectra at Max RMS (Locations 1-4)

4.7 Velocity Profiles

Data from the hot-wire campaign yielded mass flux fluctuations. To estimate fluctuations in the streamwise velocity component from the fluctuations in the mass flux, several assumptions are made[21,67]. First, following Morkovin's[52] Strong Reynolds Analogy, it is assumed that T_0' is small in comparison to T'. Using this relation, T' can be related to u' by

$$\frac{T'}{\bar{T}} = -\left(\gamma - 1\right) M^2 \frac{u'}{\bar{U}} \tag{4.5}$$

Then, if the pressure fluctuations are small compared to the temperature fluctuations, which is typical of many flows without strong perturbations, an expression relating u' and $(\rho u)'$ can be found. The resulting relation becomes

$$\frac{u'}{\bar{U}} = \frac{(\rho u)'}{\bar{\rho}\bar{U}} \left[1 + \left(\gamma - 1\right) M^2\right]^{-1} \tag{4.6}$$

When applied to the current data (using hot-wire mass flux and fluctuations, cold-wire temperature, velocity from temperature and Mach number, and Mach number from pitot probe), the resulting velocity fluctuations can be calculated. Shown in Figure 4.24 are the velocity profile and velocity fluctuations throughout the boundary layer at location 4 along the centerline. Note how the velocity profile has a straight and well defined freestream region, a characteristic absent from the Mach number profiles that have a "tail." It would appear that the use of the temperature profiles with the Mach profiles generate this result. The velocity fluctuations are near 0 in the freestream (as one would expect), and increase in magnitude down through the boundary layer. This trend is expected, and if lower portions of the boundary layer could be reached, the fluctuations would eventually begin to diminish again.

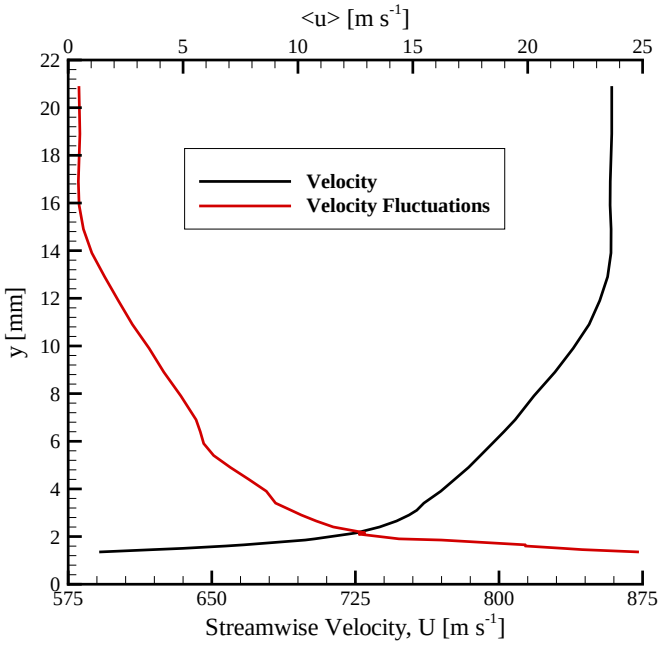

Figure 4.24: Velocity & Fluctuations (From SRA)

Shown in Figure 4.25, the scaled velocity fluctuations appear to reach 3% at the peak. When the Morkovin scaling factor is applied, Figure 4.26, the fluctuation levels across the boundary layer are revealed. While the profile is qualitatively similar to those of Kistler[35], Klebanoff, and Williams[79], the current data are significantly lower in magnitude. Since it is believed that the density profile, wall density, and friction velocity values are all within reason, the error must lie either with the velocity fluctuations calculated from the SRA, or the Morkovin scaling factor. When the data are compared to that of Kistler[35], which removes the density scaling factor and only uses friction velocity, the current data are still a factor of two lower in magnitude. Therefore, it is currently believed that the SRA assumptions (primarily that the pressure fluctuations are negligible) are not valid for this experiment.

Performing a spectral analysis on the newly decomposed velocity fluctuations, the PSD plots in Figure 4.27 were created. These spectra do not show the same

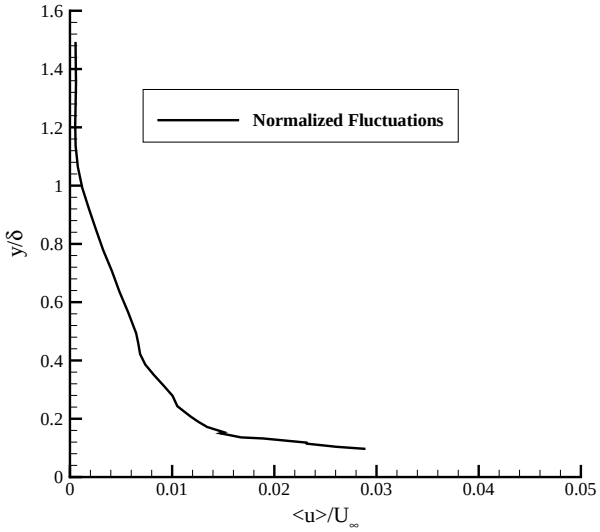

Figure 4.25: Scaled Velocity Fluctuations (From SRA)

damping near the wall as the mass flux fluctuation spectra do. Indeed, the spectra continue to increase in amplitude from the freestream values, to the highest point at the closest measurement location to the wall.

Similarly to the spectra from mass flux fluctuations, the velocity fluctuation spectra can be fit with a power law curve approximation. The results in Figure 4.28 show the effectiveness of this curve fit. Again, it would appear that the Kolmogorov scaling holds for the velocity fluctuations.

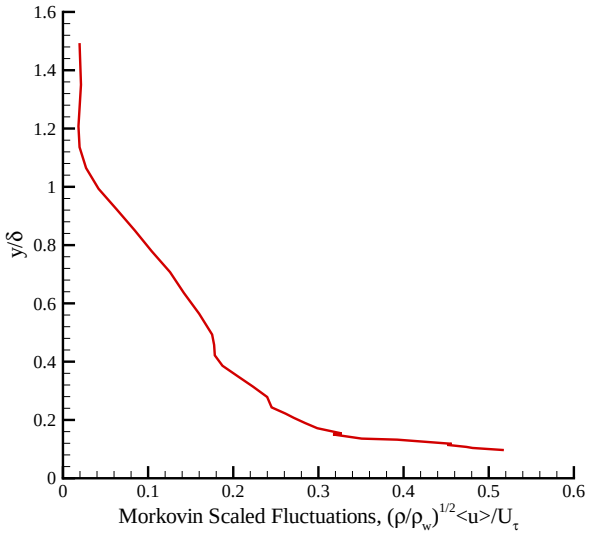

Figure 4.26: Morkovin Scaled Velocity Fluctuations

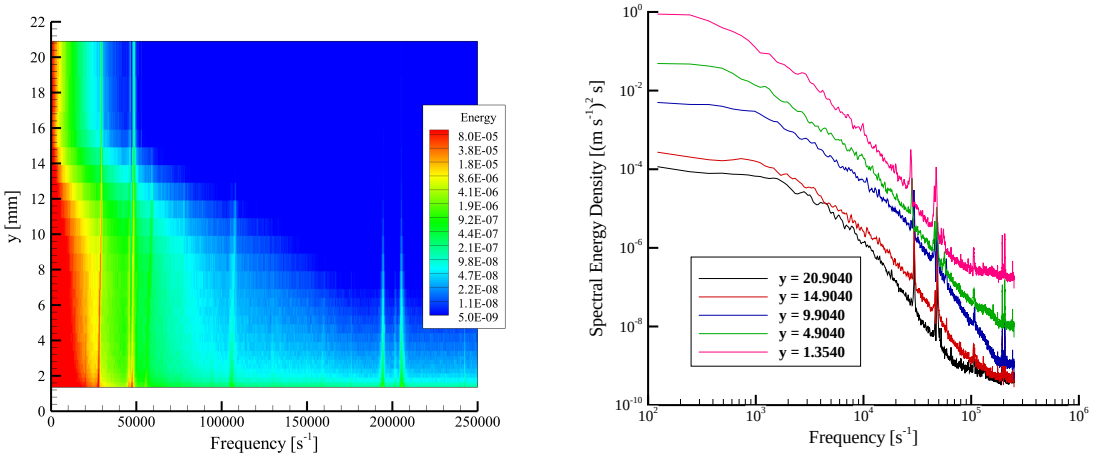

(a) Power Spectra

(b) Power Spectra (Selected Heights)

Figure 4.27: Power Spectra of Velocity Fluctuations (Location 4, Tripped)

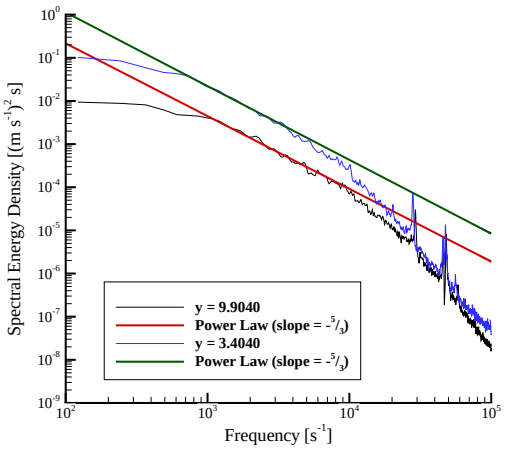

(a) Power Law Fit, Velocity Fluctuations (Frequency)

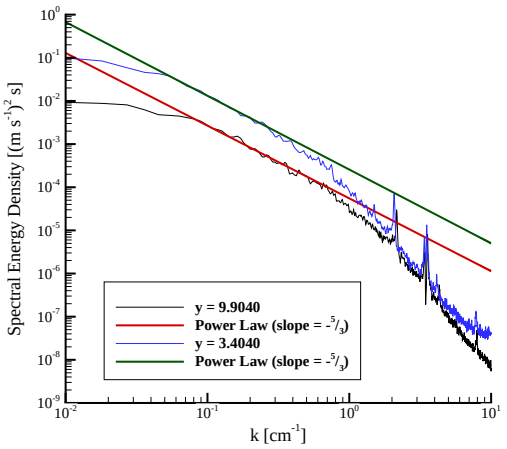

(b) Power Law Fit, Velocity Fluctuations (Wavenumber)

Figure 4.28: Turbulence Power Spectra Scaling, Velocity Fluctuations

5. CONCLUSIONS AND RECOMMENDATIONS

5.1 Conclusions

The purpose of the current study was to answer several questions related to hypersonic, low Reynolds number, turbulent boundary layers. To that end, a unique research facility was created, instrumentation was developed to acquire data in the challenging low Reynolds number (low density) domain, and meaningful data was collected and analyzed. The boundary layer examined in this experiment resembled other, higher Reynolds number boundary layers, but also exhibited its own unique characteristics.

5.1.1 Scaling Laws

The data acquired from the pitot probe surveys were scaled to inner variables using the classical methods of the law of the wall derivation. As expected, the original variables did not follow the law of the wall. When transformed using the method of Van Driest, however, which accounts for variable density, the variables were able to match the laminar sublayer and log layer regions. Noticeably absent from the data was an overlap region between the two layers, which suggests a different profile for the velocity profiles at these low Reynolds number, hypersonic conditions. The Crocco-Busemann relation was found to provide satisfactory results under its general assumptions.

The hot-wire data (mass flux fluctuations) were converted to streamwise velocity fluctuations using the Strong Reynolds Analogy. The velocity fluctuations were then scaled using the method of Morkovin, which involves the density profile, wall density, and friction velocity. When compared to available data, the current results fell almost an order of magnitude short. Having strong confidence in the friction velocity

(from the accuracy of the law of the wall data), and the density profile (from the temperature profile measurements and wall pressure measurements), the only sources for error are in the Strong Reynolds Analogy decomposition, or the Morkovin scaling. The Strong Reynolds Analogy's applicability to hypersonic flows is dubious, but has not been categorically rejected. It is possible that the large variation of density across the boundary layer (Morkovin scaling is based on the ratio of ρ/ρ_w) has a strong effect on the scaled quantities.

5.1.2 Two Dimensionality

As the oil flows of the entire model suggest, the trips seem to promote uniformity across the span of the model. The disorganized oil flow of the untripped case is almost completely gone when compared to the tripped case. Such a change in uniformity is preferential when discussing inlets to air-breathing propulsion systems.

When comparing spanwise profiles of mass flux and Mach number, there appears to be generally good agreement of the data. There are some areas, however, that show a departure from the majority of the data. These areas can be attributed to several things, including: model misalignment which creates a spanwise pressure gradient, wake instabilities (generated by the trips), or wake merging as downstream distance is increased. Additional information is needed to determine if two-dimensional simulations are sufficient for these boundary layers.

5.1.3 Turbulent Power Spectra

Turbulence is composed of an enormous amount of length scales, ranging from large scales on the order of the boundary layer, to the smallest scales corresponding to energy dissipation due to viscous effects. Kolmogorov investigated these scales from a dimensional analysis, and determined that due to the cascade of energy through the length scales, the power spectra of a turbulent boundary layer should follow a power

law with a slop of approximately $-5/3$. When the current boundary layer under investigation is analyzed using a Fourier transform, the resulting spectra is found to follow this power law. This result verifies that even at low Reynolds numbers, the length scales still follow the behavior described by Kolmogorov.

5.1.4 Near Wall Turbulence

Using the pitot probe data, the current study was able to reach the lower 10% of the boundary layer, or a y^+ of approximately 10. The results from the law of the wall analysis show that the final few data points may be in the laminar sublayer - a region where the two scaled variables vary linearly. However, the transition from the laminar sublayer to the log layer occurs in a manner different than that predicted by theory. The low density effects near the wall may be having an effect on the turbulence that modifies this region in a manner not currently anticipated.

5.1.5 Disturbance Growth Rates

By probing the boundary layer at four distinct downstream locations, the evolution of the disturbances and the boundary layer state was determined. It is well known that the trips currently used create a pair of counter-rotating vortices that generate upwash and downwash regions in their wakes. These wakes create disturbances in the boundary layer that cause transition from laminar flow to turbulent. As the probe is moved downstream of the trips, the peak RMS disturbance value grows in amplitude until it reaches some critical value. After this point, the peak begins to decrease in amplitude, but the affected region spreads throughout the boundary layer. Once the influenced region covers a significant portion of the boundary layer, transition occurs.

5.2 Recommendations

The current experiment provided both technical and scientific contributions. A new facility for future experiments was created, and the supporting instrumentation was also developed. The current study provided insight into low Reynolds number, hypersonic turbulent boundary layers.

However, there are some questions that were not completely answered, and some new questions raised from the data. To address these issues, the following recommendations for future work are made.

The influence of sidewall boundary layers caused a "channeling" of the streamlines on the plate. Using a tapered plate would eliminate this influence and remove some uncertainty in the measurements.

The multiple overheat ratio hot-wire data is widely scattered, and this is believed to be a direct effect of performing the scans during different runs. To eliminate this problem, a hot-wire scanning circuit should be employed. This circuit would cycle through a set amount of available overheat ratios during a run at each point in the boundary layer, thus ensuring the conditions were nearly constant.

The Mach number profiles were converted to law of the wall plots using measured quantities, with the exception of wall shear stress, which was chosen to match the inner layer of the data. Using a Preston tube (the tube used in the current study was not a true Preston tube) at each spanwise location would yield wall shear stress, and could correct all of the data to have even better agreement.

The current traverse system can only move in a single axis for a given experiment. Developing a two-axis traverse, or even moving the traverse to perform spanwise surveys would help reveal information about the periodicity of the trip wakes (measuring at different streamwise and different boundary layer heights) and the uniformity of

the boundary layer created by the trips. Also, traversing in the streamwise direction at given boundary layer heights would provide additional insight into the transition process.

As an alternative to oil flow, the phosphor thermography technique developed by NASA and used by Berry et al. could reveal the streamline characteristics of the trips more accurately[7]. This technique would also reveal the transition location by locating the area of increased temperature.

Moving forward, there are also some suggestions for not only improvements on the current study, but future studies in this facility. Similar to Tichenor[72] et al., experiments can be conducted to determine the effect of mechanical non-equilibrium effects (favorable pressure gradients, adverse pressure gradients, distributed roughness, etc.) on the turbulence properties in a low Reynolds number environment. With viscous effects having a more pronounced role in this flow regime, the results may prove to be quite different from previous research at higher Reynolds numbers. Similarly, the effects of thermal non-equilibrium (rotational/vibrational/electronic/ excitation) may show interesting phenomena in a flow field where collision driven relaxation is not as dominant. The flow of energy through the internal states of the fluid may be markedly different at conditions where density approaches that of realistic flight vehicles.

REFERENCES

[1] Aerosoft. *GASP Version 4.0 Users' Manual*. Aerosoft, Inc., Blacksburg, Virginia, 2001.

[2] John D. Anderson, Jr. *Hypersonic and High Temperature Gas Dynamics*. AIAA, Reston, VA, 2000.

[3] R.P. Bartlett, A.J. Edwards, J.K. Harvey, and R. Hillier. Pitot pressure and total temperature profile measurements in a hypersonic turbulent boundary layer at M=9. Technical Report Rep. 79-01, I.C. Aero, 1979.

[4] B.F. Bathel, P.M. Danehy, J.A. Inman, A.N. Watkins, S.B. Jones, W.E. Lipford, K.Z. Goodman, C.B. Ivey, and C.P. Goyne. Hypersonic laminar boundary layer velocimetry with discrete roughness on a flat plate. *AIAA Journal*, 49(9):1883–1896, 2011.

[5] M.L. Baumgartner. *Turbulence Structure in a Hypersonic Boundary Layer*. PhD thesis, Princeton University, Princeton, NJ, 1997.

[6] D.E. Berg. *Surface Roughness Effects on the Hypersonic Turbulent Boundary Layer*. PhD thesis, CALTECH, Pasadena, CA, 1977.

[7] S.A. Berry, A.H. Auslender, A.D. Dilley, and J.F. Calleja. Hypersonic boundary-layer trip development for Hyper-X. *Journal of Spacecraft and Rockets*, 38(6):853–864, 2001.

[8] M. Bertram. Investigation of the pressure-ratio requirements of the Langley 11-inch hypersonic tunnel with a variable-geometry diffuser. Technical Report NACA RM L50I13, NACA, October 1952.

[9] P. Bookey, M. Wu, A.J. Smits, and P. Martin. New experimental data of STBLI at DNS/LES accessible Reynolds numbers. Reno, NV, 2005. AIAA Conference. AIAA Paper 2005-0309.

[10] M.P. Borg, S.P. Schneider, and T.J. Juliano. Effect of freestream noise on roughess-induced transition for the X-51A forebody. Reno, NV, January 2008. AIAA Conference. AIAA Paper 2008-0592.

[11] Rodney Dale Welch Bowersox. *Compressible Turbulence in a High-speed High Reynolds Number Mixing Layer*. PhD thesis, Virginia Polytechnic Institute and State University, Blacksburg, VA, 1992.

[12] P. Bradshaw. *An Introduction to Turbulence and Its Measurement*. Pergamon Press, Oxford, UK, 1971.

[13] H.H. Bruun. *Hot-Wire Anemometry: Principles and Signal Analysis*. Oxford University Press, New York, NY, 1995.

[14] T. Cebeci and A.M.O. Smith. *Analysis of Turbulent Boundary Layers*. Academic Press, Inc., New York, NY, 1974.

[15] H.K. Cheng. Perspectives on hypersonic viscous flow research. *Annual Review of Fluid Mechanics*, 25:455–484, 1993.

[16] M. Choudhari, F. Li, M. Wu, C. Chang, J. Edwards, M. Kegerise, and R. King. Laminar-turbulent transition behind discrete roughness elements in a high-speed boundary layer. Orlando, FL, 2010. AIAA Conference. AIAA Paper 2010-1575.

[17] J.E. Danberg. Measurements of the characteristics of the compressible turbulent boundary layer with air injection. Technical Report Rep. 6683, NOL NAVORD, 1960.

[18] J.E. Danberg. Characteristics of the turbulent boundary layer with heat and mass transfer: Data tabulation. Technical Report NOLTR 67-6, NOL, 1967.

[19] A. Demetriades and A.J. Laderman. Reynolds stress measurements in a hypersonic boundary layer. *AIAA Journal*, 11:1594–1596, 1973.

[20] C. Forbes Dewey, Jr. Hot-wire measurements in low reynolds number hypersonic flows. Technical Report Memorandum No. 63, Guggenheim Aeronautical Laboratory California Institute of Technology, September 1961.

[21] J.F. Donovan and E.F. Spina. An improved analysis method for cross-wire signals obtained in supersonic flow. *Experiments in Fluids*, 12:359–368, 1992.

[22] H.H. Fernholz and P.J. Finley. A critical compilation of compressible turbulent boundary layer data. Technical Report AGARD-AG-223, AGARD, 1977.

[23] H.H. Fernholz and P.J. Finley. A further compilation of compressible boundary layer data with a survey of turbulence data. Technical Report AGARD-AG-263, AGARD, 1981.

[24] M.C. Fischer and D.V. Maddalon. Experimental laminar, transitional, and turbulent boundary layer profiles on a wedge at local Mach number 6.5 and comparisons with theory. Technical Report D-6462, NASA, 1971.

[25] M.C. Fischer, D.V. Maddalon, L.M. Weinstein, and R.D. Wagner. Boundary-layer surveys on a nozzle wall at M=20 including hot-wire fluctuation measurements. Los Angeles, CA, 1970. AIAA Conference. AIAA Paper 70-746.

[26] M.C. Fischer, D.V. Maddalon, L.M. Weinstein, and R.D. Wagner. Boundary-layer pitot and hot-wire surveys at M=20. *AIAA Journal*, 9:826–834, 1971.

[27] J.O. Hinze. *Turbulence, an Introduction to its Mechanism and Theory.* McGraw-Hill, New York, NY, 1959.

[28] E.J. Hopkins and E.R. Keener. Study of surface pitots for measuring turbulent skin friction at supersonic Mach numbers - adiabatic wall. Technical Report D-3478, NASA, 1966.

[29] R.A. Humble, S.J. Peltier, and R.D.W. Bowersox. Visualization of the structural response of a hypersonic turbulent boundary layer to convex curvature. *Physics of Fluids*, 24, 2012.

[30] E.R. Keener and E.J. Hopkins. Use of preston tubes for measuring hypersonic turbulent skin friction. Technical Report D-5544, NASA, 1969.

[31] E.R. Keener and E.J. Hopkins. Turbulent boundary layer velocity profiles on a nonadiabatic flat plate at Mach number 6.5. Technical Report D-6907, NASA, 1972.

[32] M.A. Kegerise, L.R. Owens, and R.A. King. High-speed boundary-layer transtion induced by an isolated roughness element. Chicago, IL, 2010. AIAA Conference. AIAA Paper 2010-4999.

[33] J.H. Kemp and F.K. Owen. Nozzle wall boundary layer at Mach numbers 20 to 47. *AIAA Journal*, 10:872–879, 1972.

[34] J.M. Kendall. Wind tunnel experiments relating to supersonic and hypersonic boundary-layer transition. *AIAA Journal*, 13(3):290–299, 1975.

[35] A.L. Kistler. Fluctuation measurements in a supersonic turbulent boundary layer. *Physics of Fluids*, 2(1):290–296, 1959.

[36] A.N. Kolmogorov. The local structure of turbulence in incompressible viscous fluid for very large Reynolds numbers. *Proceedings of the USSR Academy of Sciences*, 30:299–303, 1941.

[37] L.S.G. Kovasznay. Turbulence in supersonic flow. *Journal of the Aeronautical Sciences*, 20(10):657–674, 1953.

[38] A.J. Laderman. New measurements of turbulent shear stresses in hypersonic boundary layers. *AIAA Journal*, 14:1286–1291, 1976.

[39] A.J. Laderman and A. Demetriades. Hot-wire measurements of hypersonic boundary layer turbulence. *Physics of Fluids*, 16:179–181, 1973.

[40] A.J. Laderman and A. Demetriades. Mean and fluctuating flow measurements in the hypersonic boundary layer over a cooled wall. *Journal of Fluid Mechanics*, 63:121–144, 1974.

[41] J.F. Lafferty and J.D. Norris. Measurements of fluctuating pitot pressure 'tunnel noise,' in the AEDC hypervelocity wind tunnel No. 9. Destin, FL, 2007. AIAA Conference. AIAA Paper 2007-1678.

[42] R.E. Lee, W.J. Yanta, and A.C. Leonas. Velocity profile, skin-friction balance and heat-transfer measurements of the turbulent boundary layer at Mach 5 and zero-pressure gradient. Technical Report 69-106, United States Naval Ordnance Laboratory, White Oak, Maryland, June 1969.

[43] D. Masutti, E. Spinosa, O. Chazot, and M. Carbonaro. Disturbance level characterization of a hypersonic blowdown facility. *AIAA Journal*, 50(12):2720–2730, 2012.

[44] P. Materna. Hot wire anemometry in a hypersonic turbulent boundary layer. Albuquerque, NM, 1977. AIAA Conference. AIAA Paper 77-702.

[45] C.B. McGinley, E.F. Spina, and M. Sheplak. Turbulence measurements in a Mach 11 helium boundary layer. Colorado Sprigns, CO, 1994. AIAA Conference. AIAA Paper 94-2364.

[46] F.R. Menter. Zonal two equation k-ω turbulence models for aerodynamic flows. Orlando, FL, 1993. AIAA Conference. AIAA Paper 93-2906.

[47] V. Mikulla and C.C. Horstman. The measurement of shear stress and total heat flux in a nonadiabatic turbulent hypersonic boundary layer. Pasadena, CA, 1975. AIAA Conference. AIAA Paper 75-119.

[48] V. Mikulla and C.C. Horstman. Turbulence stress measurements in a nonadiabatic hypersonic boundary layer. *AIAA Journal*, 13:1607–1613, 1975.

[49] V. Mikulla and C.C. Horstman. Turbulence measurements in hypersonic shock-wave boundary-layer interaction flows. *AIAA Journal*, 14:568–575, 1976.

[50] D.R. Moore. *Velocity Similarity in the Compressible Turbulent Boundary Layer with Heat Transfer*. PhD thesis, Univ. of Texas, Austin, TX, 1962. DRL-480.

[51] M. Morkovin, E. Reshotko, and T. Herbert. Transition in open flow systems - a reassessment. *Bull. American Physics Society*, 39:1882, 1994.

[52] M.V. Morkovin. Effects of compressibility on turbulent flow. In *Mecanique de la Turbulence*, pages 367–380. Gordon and Breach, London, UK, 1962.

[53] F.K. Owen. Turbulence and shear stress measurements in hypersonic flow. Reno, NV, 1990. AIAA Conference. AIAA Paper 90-1394.

[54] F.K. Owen and C.C. Horstman. On the structure of hypersonic turbulent boundary layers. *Journal of Fluid Mechanics*, 53:611–636, 1972.

[55] F.K. Owen, C.C. Horstman, and M.I. Kussoy. Mean and fluctuating flow measurements of a fully-developed, non-adiabatic hypersonic boundary layer. *Journal of Fluid Mechanics*, 70:393–413, 1975.

[56] F.K. Owen, C.C. Hortstman, P.C. Stainback, and R.D. Wagner. Comparison of wind tunnel transition and freestream disturbance measurements. *AIAA Journal*, 13(3):266–269, 1975.

[57] A. Pope and K. Goin. *High-Speed Wind Tunnel Testing*. Krieger Publishing, Malabar, FL., 1965.

[58] M.J. Ringuette, M.P. Martin, and A.J. Smits. Characterization of the turbulence structure in supersonic boundary layers using DNS data. San Francisco, CA, 2006. AIAA Conference. AIAA Paper 2006-3539.

[59] M.J. Ringuette and A.J. Smits. Wall-pressure measurements in a Mach 3 shock-wave turbulent boundary layer interaction at a DNS accessible Reynolds number. Miami, FL, 2007. AIAA Conference. AIAA Paper 2007-4113.

[60] D. Sahoo, M.J. Ringuette, and A.J. Smits. Experimental investigation of a hypersonic turbulent boundary layer. Orlando, FL, 2009. AIAA Conference. AIAA Paper 2009-0780.

[61] P. Schlatter and R. Örlü. Turbulent boundary layers at moderate Reynolds numbers: inflow length and tripping effects. *Journal of Fluid Mechanics*, 710:5–34, 2012.

[62] M. Semper, B. Pruski, and R. Bowersox. Freestream turbulence measurements in a continuously variable hypersonic wind tunnel. Nashville, TN, January 2012. AIAA Conference. AIAA Paper 2012-0732.

[63] M. Semper, N. Tichenor, R. Bowersox, Srinvasan R., and S. North. On the design and calibration of an actively controlled expansion hypersonic wind tunnel. Orlando, FL, January 2009. AIAA Conference. AIAA Paper 2009-799.

[64] G.S. Settles. *Schlieren and Shadowgraph Techniques: Visualizing Phenomena in Transparent Media*. Springer, New York, NY, 2001.

[65] J.A. Smith and J.F. Driscoll. The electron-beam fluorescence technique for measurements in hypersonic turbulent flows. *Journal of Fluid Mechanics*, 72:695–720, 1975.

[66] P.R. Spalart and S.R. Allmaras. A one equation turbulence model for aerodynamic flows. Reno, NV, 1992. AIAA Conference. AIAA Paper 92-0439.

[67] E.F. Spina, J.F. Donovan, and A.J. Smits. On the structure of high-Reynolds number supersonic turbulent boundary layers. *Journal of Fluid Mechanics*, 222:293–327, 1991.

[68] K.F. Stetson. Hypersonic transition testing in wind tunnels. In *Instability and Transition*, pages 91–97. Springer, New York, NY, 1990.

[69] P.K. Subbareddy and G.V. Candler. DNS of transition to turbulence in a Mach 6 boundary layer. New Orleans, LA, June 2012. AIAA Conference. AIAA Paper 2012-3106.

[70] H. Tennekes and J.L. Lumley. *A First Course in Turbulence*. MIT Press, Cambridge, MA, 1972.

[71] N. Tichenor, M. Semper, R.D.W. Bowersox, R. Srinvasan, and S.W. North. Calibration of an actively controlled expansion hypersonic wind tunnel. Chicago, IL, June 2010. AIAA Conference. AIAA Paper 2010-4793.

[72] N.R. Tichenor, R.A. Humble, and R.D.W. Bowersox. Response of a hypersonic turbulent boundary layer to favourable pressure gradients. *Journal of Fluid Mechanics*, 722:187–213, 2013.

[73] E. Van Driest. Turbulent boundary layer in compressible fluids. *Journal of Aerospace Sciences*, pages 145–160, 1951.

[74] T. von Kármán. Turbulence. twenty-fifth wilbur wright memorial lecture. *Joural of Royal Aeronautics*, 41:1109, 1937.

[75] R.D. Watson, J.E. Harris, and J.B. Anders. Measurements in a transitional/turbulent Mach 10 boundary layer at high Reynolds numbers. Washington, DC, 1973. AIAA Conference. AIAA Paper 73-165.

[76] P. Wegener and K. Lobb. An experimental study of a hypersonic wind-tunnel diffuser. *Journal of Aeronautical Sciences*, 20:105–110, Feb. 1953.

[77] Frank M. White. *Viscous Fluid Flow*. McGraw-Hill, New York, NY, 3rd edition, 2006.

[78] D.C. Wilcox. *Turbulence Modeling for CFD*. DCW Industries, La Canada, CA, 2nd edition, 1998.

[79] O. Williams and A. Smits. Tripping of boundary layers in hypersonic flow. Gananoque, Ontario, 2012. 1000 Islands Fluid Mechanics Meeting.

[80] E.M. Winkler and M.H. Cha. Investigation of flat plate hypersonic turbulent boundary layers with heat transfer at a Mach number of 5.2. Technical Report Rep 6631, NOL NAVORD, 1959.

APPENDIX A

DERIVATION OF HOT-WIRE RESPONSE EQUATION

The following derivation borrows from and follows the steps outlined in Reference[11], with the exception of deriving the formulas for an arbitrary power of n in the Reynolds number relationship to Nusselt number. Traditionally, this exponent is usually approximated as $^1/_2$.

For turbulent compressible flow, the dimensionless heat transfer, the Nusselt number, of a cylinder has the following functional form

$$Nu = f(L/d, M, Pr, Re_e, \tau). \tag{A.1}$$

L/d is the wire aspect ratio; M is the Mach number; Pr is the Prandtl number; Re_e is the effective cooling Reynolds number (based on wire diameter); and τ is the temperature loading factor, which can be expressed as $\tau = (T_w - T_e)/T_t$, where T_w is the wire temperature, and T_e is the temperature the unheated wire would attain if placed in the flow, called the equilibrium temperature. For Reynolds numbers greater than about 20, T_e is about 97% of T_t. For flows where the Mach number normal to the wire is greater than about 1.2, or $M \sin\phi \geq 1$; Pr is constant; and the aspect ratio $\gg 1$, then Eqn. A.1 reduces to

$$Nu = f(Re_e, \tau). \tag{A.2}$$

Experimentally, the data has been found to collapse onto the following curve (for wires normal to the flow)

$$Nu = \left(aRe^n + b\right)\left(1 - c\tau\right), \tag{A.3}$$

where traditionally the exponent n is equal to 0.5 for compressible flows and the value $c\tau$ is usually neglected (this results in a calibration needing to be done at each overheat).

The Nusselt number is defined here as

$$Nu = \frac{q_w}{\pi k_t L\left(T_w - T_e\right)}, \tag{A.4}$$

where $q_w = i_w^2 R_w$ (the wire heat transfer = to the wire power). From anemometer circuit analysis $i_w = V_w / \left(R_w + R_s + R_L\right)$. Therefore, assuming the equilibrium temperature to be the same as the total temperature, which results in no error if done in both the calibration and the data reduction, the Nusselt number can be expressed as

$$Nu = \frac{V_w^2 R_w}{\left(R_w + R_s + R_L\right)^2} \frac{1}{\pi k_t L\left(T_w - T_t\right)}. \tag{A.5}$$

The thermal conductivity and viscosity are based on T_t in calculating Nu and Re. This is reasonable, since a bow shock proceeds the wire ($T_2/T_t \approx 1$), and most of the heat transfer takes place in the stagnation region. The correct temperature would be a bulk (or average) temperature based on T_t and T_2, however, this temperature would be heavily weighted to T_t, which leads to simply evaluating the thermal properties at T_t.

The viscosity was computed using the Keyes formula,

$$\mu = a_0 \times 10^{-6}\sqrt{T}/\left(1 + a_1 T_1/T\right) \qquad T_1 = 10^{-a_2/T} \tag{A.6}$$

$$\text{Air:} \quad a_0 = 1.488 \qquad a_1 = 122.1 \qquad a_2 = 5.0,$$

and the thermal conductivity was computed from a curve fit of tabulated data. However, to evaluate the turbulence equations, the functional forms for μ_t and k_t were needed. The typical power laws were incorporated, and are given by

$$k_t = k_0 \left(\frac{T_t}{T_0}\right)^{n_k} \text{and } \mu_t = \mu_0 \left(\frac{T_t}{T_0}\right)^{n_\mu}; \tag{A.7}$$

$n_\mu = 0.77$ and $n_k = 0.89$ were found to match the data satisfactorily.

Combining Equations A.3 and A.5 results in,

$$\frac{V_w^2 R_w}{\left(R_w + R_s + R_L\right)^2} \frac{1}{\pi k_t L \left(T_w - T_t\right)} = a Re_e^n + b,$$

where

$$C_0 \equiv \frac{\left(R_w + R_s + R_L\right)^2}{R_w} \pi L k_0.$$

The resulting equation becomes

$$\frac{V_w^2}{C_0} = \left(\frac{T_t}{T_0}\right)^{n_k} \left(a Re_e^n + b\right)\left(T_w - T_t\right). \tag{A.8}$$

Defining a new quantity, Reo_e, the effective Reynolds number with $\mu = \mu_0$,

$$Reo_e \equiv \frac{\rho u d}{\mu_0}$$

$$Re_e = \frac{\rho u d}{\mu_t} = \frac{\rho u d}{\mu_0}\left(\frac{T_t}{T_0}\right)^{-n_\mu} = Reo_e\left(\frac{T_t}{T_0}\right)^{-n_\mu}, \tag{A.9}$$

and substituting back into Equation A.8 gives

$$\frac{V_w^2}{C_0} = \left(\frac{T_t}{T_0}\right)^{n_k}\left[aReo_e^n\left(\frac{T_t}{T_0}\right)^{-n_\mu n} + b\right](T_w - T_t). \tag{A.10}$$

The instantaneous quantities V_w, Reo_e, and T_t are replaced by the mean plus the fluctuating component,

$$V_w = \overline{V}_w + v'_w\ ,\ \ T_t = \overline{T}_t + T'_t\ ,\ \ Reo_e = \overline{Reo}_e + Reo'_e.$$

As an example below, the following quantity becomes,

$$\left[\frac{T_t}{T_0}\right]^{n_k} = \left[\frac{1}{T_0}\right]^{n_k}\left[\overline{T}_t + T'_t\right]^{n_k} = \left[\frac{1}{T_0}\right]^{n_k}\left[\overline{T}_t\left(1 + \frac{T'_t}{\overline{T}_t}\right)\right]^{n_k}. \tag{A.11}$$

The binomial theorem is defined as

$$(x+y)^r = x^r + rx^{r-1}y + \frac{r(r-1)}{2!}x^{r-2}y^2 + ...$$

Applying the binomial theorem and neglecting higher order fluctuating terms

$$\left(1 + \frac{T'_t}{\overline{T}_t}\right)^{n_k} = 1^{n_k} + n_k(1)^{n_k-1}\left[\frac{T'_t}{\overline{T}_t}\right] = 1 + n_k\frac{T'_t}{\overline{T}_t}$$

$$\left[\frac{T_t}{T_0}\right]^{n_k} = \left[\frac{\overline{T}_t}{T_0}\right]^{n_k}\left[1 + n_k\frac{T'_t}{\overline{T}_t}\right]. \tag{A.12a}$$

Following this same expansion procedure, the remaining terms are expanded to give

$$V_w^2 = \overline{V_w}^2 + 2\overline{V_w}v'_w \tag{A.12b}$$

$$Reo_e^n = \overline{Reo_e}^n \left(1 + n\frac{Reo'_e}{\overline{Reo_e}}\right) \tag{A.12c}$$

$$\left(\frac{T_t}{T_0}\right)^{-n_\mu n} = \left(\frac{\overline{T}_t}{T_0}\right)^{-n_\mu n} \left(1 - n_\mu n\frac{T'_t}{\overline{T}_t}\right) \tag{A.12d}$$

$$(T_w - T_t) = \left[\left(T_w - \overline{T_t}\right) - T'_t\right] = \left(T_w - \overline{T_t}\right)\left[1 - M\frac{T'_t}{\overline{T}_t}\right] \tag{A.12e}$$

$$M \equiv \frac{\overline{T_t}}{T_w - \overline{T_t}}.$$

Substituting Equations A.12 back into Equation A.10 yields,

$$\begin{aligned}\frac{\overline{V_w}^2 + 2\overline{V_w}v'_w}{C_0} &= \left(\frac{\overline{T}_t}{T_0}\right)^{n_k}\left(1 + n_k\frac{T'_t}{\overline{T}_t}\right)\times \\ &\left\{a\left[\overline{Reo_e}^n\left(1 + n\frac{Reo'_e}{\overline{Reo_e}}\right)\left(\frac{\overline{T}_t}{T_0}\right)^{-n_\mu n}\left(1 - n_\mu n\frac{T'_t}{\overline{T}_t}\right)\right] + b\right\}\times \\ &\left(T_w - \overline{T_t}\right)\left(1 - M\frac{T'_t}{\overline{T}_t}\right).\end{aligned} \tag{A.13}$$

Multiplying the terms through, neglecting higher order terms, using the fact that,

$$\frac{\overline{V_w}^2}{C_0} = \left(\frac{\overline{T_t}}{T_0}\right)^{n_k} \left[a\overline{Re_e^n} + b\right]\left(T_w - \overline{T_t}\right),$$

then solving for $v'_w/\overline{V_w}$, the resulting *hot-wire fluctuation equation* can be expressed as

$$\frac{v'_w}{\overline{V_w}} = f_s \frac{Reo'_e}{\overline{Reo_e}} + g_s \frac{T'_t}{\overline{T_t}}, \tag{A.14}$$

where the *hot-wire sensitivites* are given by

$$f_s \equiv \frac{n}{2}\left(1 + \frac{b}{a\overline{Re_e^n}}\right)^{-1} \qquad and \qquad g_s \equiv \frac{-\overline{T_t}}{2\left(T_w - \overline{T_t}\right)} - n_\mu f_s + \frac{n_k}{2}. \tag{A.15}$$

For this experiment, the calibration curve fit is linear, defining $n = 1$, and the sensitivities become

$$f_s = \frac{1}{2}\left(1 + \frac{b}{a\overline{Re_e}}\right)^{-1} \qquad and \qquad g_s = \frac{-\overline{T_t}}{2\left(T_w - \overline{T_t}\right)} - n_\mu f_s + \frac{n_k}{2}. \tag{A.16}$$

If Equation A.14 is squared and averaged, the turbulence results can be computed from

$$\overline{\left(\frac{v'_w}{\overline{V_w}}\right)^2} = f_s^2 \overline{\left(\frac{Reo'_e}{\overline{Reo_e}}\right)^2} + 2 f_s g_s \overline{\left(\frac{Reo'_e}{\overline{Reo_e}}\frac{T'_t}{\overline{T_t}}\right)} + g_s^2 \overline{\left(\frac{T'_t}{\overline{T_t}}\right)^2}. \tag{A.17}$$

Equation A.17 is the basis by which the hot-wire turbulence results were calculated.